



Shape dependence and sulfate promotion of CeO₂ for selective catalytic reduction of NO_x with NH₃



Lei Ma^a, Chang Yup Seo^a, Mohit Nahata^a, Xiaoyin Chen^a, Junhua Li^{b,*}, Johannes W. Schwank^{a,*}

^a Department of Chemical Engineering, University of Michigan, Ann Arbor, MI 48109, USA

^b School of Environment, Tsinghua University, Beijing 100084, China

ARTICLE INFO

Keywords:

CeO₂ morphology
Sulfation
Solid acid
Ammonia adsorption
In situ DRIFTS

ABSTRACT

Thermally stable CeO₂ cubes and nanospheres were synthesized and modified by sulfation treatment. Non-sulfated CeO₂ cubes and nanospheres did not exhibit good catalytic performance for selective catalytic reduction of NO_x with NH₃ (NH₃-SCR), but mainly contributed towards an undesired side reaction of NH₃ oxidation above 350 °C. Based on the structural, morphological and physicochemical characterization, it was observed that CeO₂ nanospheres comprising small crystallites could easily release active oxygen species, which resulted in strong NH₃ oxidation. However, sulfation treatment greatly improved the catalytic performance of NH₃-SCR on both CeO₂ cubes and nanospheres. Sulfated CeO₂ catalysts did not contribute to significant NH₃ oxidation due to the inhibited reducibility of Ce⁴⁺ coordinated with the surface sulfates. The adsorbed ammonia could be activated on Brønsted acid sites generated by the formation of surface Ce₂(SO₄)₃ species, while gaseous NO_x could be activated on separate surface sites of Ce⁴⁺. The presence of separate reaction sites for NH₃ and NO_x is believed to be important for the improved catalytic performance of SCR reaction. Sulfated CeO₂ cubes outperformed sulfated CeO₂ nanospheres in the entire test temperature window (200–500 °C). The improved performance of sulfated CeO₂ cubes appears to be related to surfaces with abundant Brønsted acid sites and relatively weak reducibility of Ce⁴⁺. These fundamental findings contribute to a better mechanistic understanding needed for designing efficient CeO₂-based NO_x reduction catalysts in the future.

1. Introduction

Selective catalytic reduction of NO_x with NH₃ (NH₃-SCR) is a well-established technology for controlling NO_x pollution. To remove NO_x from stationary sources, the traditional industrial NH₃-SCR reaction is often catalyzed by TiO₂ supported V₂O₅ catalysts. However, some problems still persist for the use of vanadium-based NH₃-SCR catalysts, such as toxicity of vanadium, inferior performance at low temperatures, and low N₂ selectivity at high temperatures. Therefore, significant efforts have been made to develop environment-friendly NH₃-SCR catalysts for NO_x removal from stationary sources. Different kinds of metal oxides, such as CeO₂, Fe₂O₃, MnO_x etc., have attracted much attention for NO_x reduction due to their high activity and selectivity [1,2].

Ceria is one of the major oxygen storage components in three-way catalysts (TWCs), since it can rapidly switch the average oxidation state in a suitable temperature range and maintain its structural integrity [3,4]. Recent studies have indicated that supported and/or mixed CeO₂ were superior NH₃-SCR catalysts with high efficiency at relatively low temperatures [5–10]. It is believed that pure CeO₂ catalysts may not

exhibit good NH₃-SCR performance, since they also facilitate the side reaction of NH₃ oxidation [11,12]. Yet, the introduction of tungsten dopants into CeO₂ catalysts could greatly improve the catalytic activity and selectivity of NH₃-SCR reactions [5,6,13]. Detailed characterizations of CeO₂-WO₃ catalysts suggested that the key role of CeO₂ was the activation of NH₃ involved in the NH₃-SCR reaction due to the strong reducibility of Ce⁴⁺ and the abundant oxygen vacancies. Doping WO₃ components could further tune the acid properties of CeO₂ to form Brønsted acid sites on the surface, which greatly promote NH₃ adsorption [5,6,13]. Therefore, it is expected that superior ceria-based NH₃-SCR catalysts could be obtained by modifying the acidity to improve NH₃ adsorption and activation. The introduction of surface sulfates might be one of the effective ways to adjust the acidic properties of metal oxide catalysts, which could further improve the NH₃-SCR activity [11,14]. For introducing SO₄²⁻ into the system, the most commonly used methods are impregnation of (NH₄)₂SO₄, wet treatment with H₂SO₄, or treatment with gaseous SO₂ or H₂S at high temperatures [15]. The sulfated samples represent solid acids due to the existence of covalent S=O bonds in sulfur complexes formed on metal oxides [16].

* Corresponding authors.

E-mail addresses: ljunhua@tsinghua.edu.cn (J. Li), schwank@umich.edu (J.W. Schwank).

Based on innovative advances in synthesis methods, different shapes of CeO₂ nanocrystals, like nanospheres, cubes, rods, polyhedrons, etc., could be successfully synthesized [17]. From the perspective of catalysis, it is believed that the catalytic performance is strongly dependent on the shape of CeO₂ [18,19]. Herein, we employed two thermally stable CeO₂ cubes and nanospheres as NH₃-SCR catalysts. The acidity was tuned by further sulfating the nanocrystals in aqueous solutions of ammonium sulfate. The objective of this work is to understand the structural dependence of CeO₂ and the effect of sulfation on the activity and selectivity of NH₃-SCR. The textural, structural, and surface properties of as-prepared samples were characterized in detail. The reproducibility and the acid strength and amount were quantified and correlated with catalytic performance. The results demonstrate that NH₃-SCR activity of CeO₂ depends on the shape and the degree of sulfation over a wide reaction temperature window. The detailed reaction mechanisms were also elucidated based on FTIR studies and correlated to the characterization data to explain the structure-activity relationship.

2. Experimental

2.1. Preparations of catalysts

The synthesis procedures of CeO₂ cubes and nanospheres were described in detail in the literature [20–23]. Both catalysts were prepared in Teflon lined hydrothermal synthesis autoclave reactor. The as-prepared CeO₂ cubes and nanospheres were finally calcined in static air at 500 °C for 4 h with a ramp rate of 2 °C/min. The sulfated CeO₂ samples with about 4 wt.% sulfur were prepared by wet impregnation of pure CeO₂ supports in aqueous solutions of (NH₄)₂SO₄. Typically, required amounts of (NH₄)₂SO₄ were dissolved in 100 mL deionized water under vigorous agitation. 2.9 g CeO₂ nanocrystals were then gradually added to the aqueous solution. After mixing, the slurry was vigorously stirred for approximate 10 h. The obtained solid samples were dried overnight at 110 °C, and again calcined in static air at 500 °C for 4 h with a ramp rate of 2 °C/min. All the samples were pressed into pellets and sieved to obtain particles with a size range of 180–250 μm before performing catalytic activity tests. CeO₂ cubes and nanospheres were denoted as CeO₂-C and CeO₂-NS, respectively. Similarly, sulfated CeO₂ cubes and nanospheres were denoted as S/CeO₂-C and S/CeO₂-NS, respectively. The chemical compositions of the catalysts are determined by inductively coupled plasma optical emission spectroscopy (ICP-OES) with an IRIS Intrepid II XSP apparatus (Thermo Fisher Scientific), and the results have been summarized in Table 1.

2.2. Catalytic activity test

Catalytic activity tests were performed in a fixed-bed quartz tube reactor of 4 mm internal diameter containing CeO₂ or sulfated CeO₂ catalysts (100 mg, 180–250 μm). The concentration of NH₃, NO_x (NO_x = NO + NO₂), and N₂O in the inlet and outlet gas was measured by Antaris™ IGS Gas Analyzer from Thermo Fisher Scientific Inc. A reactant gas mixture containing 550 ppm NO (when used), 550 ppm

NH₃ (when used), 10% O₂, and balance N₂ was passed through the bench blending reactor. In the tests, the total flow rate was fixed at 150 ml/min under standard temperature and pressure, corresponding to a weight hourly space velocity (WHSV) of 90,000 mL g⁻¹ h⁻¹. The activity test data were recorded after the reactions had reached stable states to avoid the impact of gas adsorption on the catalysts.

The catalytic performance of NH₃-SCR reaction is presented in terms of NO_x conversion (X(NO_x)) and selectivity towards N₂ (S(N₂)) as defined by Eqs. (1) and (2), respectively.

$$X(\text{NO}_x) = \frac{[\text{NO}_x]_{\text{inlet}} - [\text{NO}_x]_{\text{outlet}}}{[\text{NO}_x]_{\text{inlet}}} \times 100\% \quad (1)$$

$$S(\text{N}_2) = \left(1 - \frac{2[\text{N}_2\text{O}]_{\text{outlet}}}{[\text{NO}_x]_{\text{inlet}} + [\text{NH}_3]_{\text{inlet}} - [\text{NO}_x]_{\text{outlet}} - [\text{NH}_3]_{\text{outlet}}} \right) \times 100\% \quad (2)$$

The catalytic performance of NH₃ oxidation reaction is presented in terms of NH₃ conversion (X(NH₃)) and selectivity towards N₂ (S(N₂)), N₂O (S(N₂O)), NO_x (S(NO_x)) as defined by Eqs. (3)–(6), respectively.

$$X(\text{NH}_3) = \frac{[\text{NH}_3]_{\text{inlet}} - [\text{NH}_3]_{\text{outlet}}}{[\text{NH}_3]_{\text{inlet}}} \times 100\% \quad (3)$$

$$S(\text{N}_2) = \left(1 - \frac{2[\text{N}_2\text{O}]_{\text{outlet}} + [\text{NO}_x]_{\text{outlet}}}{[\text{NH}_3]_{\text{inlet}} - [\text{NH}_3]_{\text{outlet}}} \right) \times 100\% \quad (4)$$

$$S(\text{N}_2\text{O}) = \frac{2[\text{N}_2\text{O}]_{\text{outlet}}}{[\text{NH}_3]_{\text{inlet}} - [\text{NH}_3]_{\text{outlet}}} \times 100\% \quad (5)$$

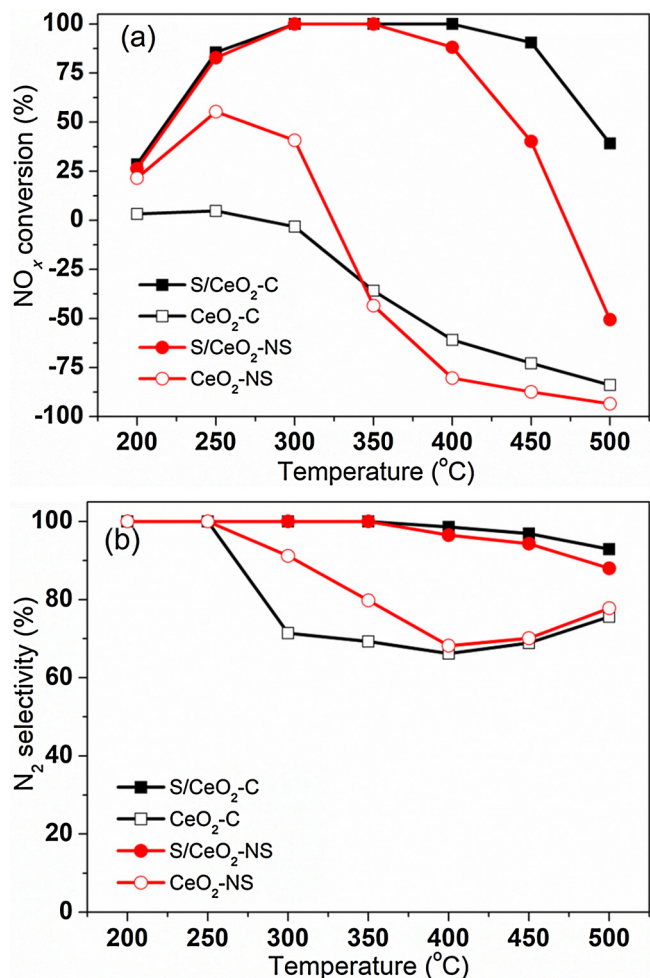


Fig. 1. Catalytic performance of SCR reaction over different catalysts. (a) NO_x conversions; (b) N₂ selectivity. Reaction conditions: 550 ppm NO, 550 ppm NH₃, 10% O₂, balance N₂, and WHSV = 90,000 mL g⁻¹ h⁻¹.

Table 1

Sulfur contents and structural parameters of different samples.

Catalysts	Sulfur contents (wt%) ^a	BET surface area (m ² /g)	Pore volume (cm ³ /g)	Average crystallite size (nm) ^b
CeO ₂ -C	–	40.7	0.14	16.4
S/CeO ₂ -C	3.2	15.8	0.07	17.7
CeO ₂ -NS	–	135.4	0.38	7.7
S/CeO ₂ -NS	4.4	27.8	0.19	10.4

^a Sulfur contents were determined by ICP-OES methods.

^b Calculated by XRD results according to Scherrer equation using FWHM of the (111) peak of CeO₂.

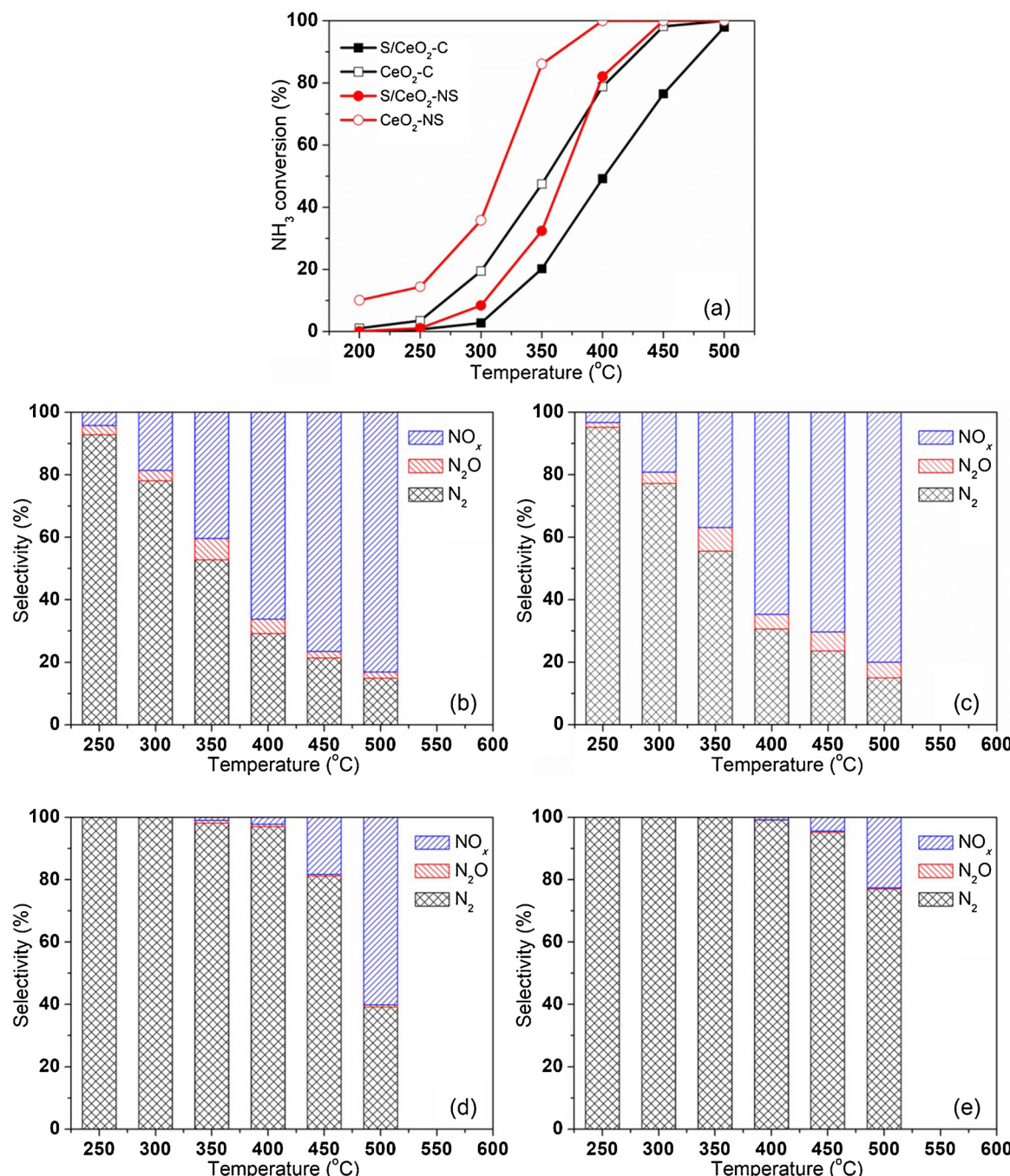


Fig. 2. Catalytic activity of NH₃ oxidation (a) and the selectivity of different products over (b) CeO₂-NS; (c) CeO₂-C; (d) S/CeO₂-NS; (e) S/CeO₂-C catalysts. Reaction conditions: 550 ppm NH₃, 10% O₂, balance N₂, and WHSV = 90,000 mL g⁻¹ h⁻¹.

$$S(\text{NO}_x) = \frac{[\text{NO}_x]_{\text{outlet}}}{[\text{NH}_3]_{\text{inlet}} - [\text{NH}_3]_{\text{outlet}}} \times 100\% \quad (6)$$

2.3. Characterizations

Transmission electron microscopy (TEM) was performed on a JEOL 3011 instrument with an acceleration voltage of 300 kV. High-resolution transmission electron microscopy (HRTEM) and energy dispersive spectroscopy (EDS) elemental mapping were performed on FEI Tecnai G² F20 S-TWIN with an acceleration voltage of 200 kV. Powder X-ray diffraction (XRD) measurements were carried out on Rigaku D/Max 2500 X-Ray Diffractometer with CuK α radiation. N₂ adsorption-desorption experiments were carried out on a Micromeritics ASAP 2020

instrument at 77 K, after sample degassing under vacuum at 350 °C with a ramp rate of 5 °C/min for 12 h.

Thermo-gravimetric (TG) analysis was performed on TA Q500 apparatus from TA Instruments. The experiment was carried out under N₂ flow (100 ml/min) and the temperature increased from 100 °C to 850 °C with a heating rate of 10 °C/min post sample pretreatment under N₂ (100 ml/min) at 100 °C for 2 h.

X-ray Photoelectron Spectroscopy (XPS) experiments were carried out on a Thermo Scientific Escalab 250Xi equipped with a monochromatic Al X-ray source. Binding energies of all the elements were calibrated relative to the adventitious carbon with C1s at 284.8 eV.

Temperature-programmed reduction by H₂ (H₂-TPR) was performed on a ChemBET-3000 from Quantachrome Instruments. Typically, 20 mg of sample was loaded in a U-shaped quartz reactor and pretreated in a

flow of N_2 (100 ml/min) at 300 °C for 1 h to remove adsorbed water and other impurities. The sample was then cooled down to room temperature in a flow of nitrogen. After the baseline was stabilized in a flow of 5% H_2/Ar (50 ml/min), the sample was heated from room temperature to 900 °C with a ramp rate of 10 °C/min. Response signals of the thermal conductivity detector (TCD) were calibrated using high-purity CuO (Sigma Aldrich) with an assumption of stoichiometric reduction of CuO by H_2 .

Temperature-programmed desorption (TPD) was conducted using 100 mg of catalyst in a quartz reactor. The adsorption was performed by feeding a gas mixture with 550 ppm NH_3 or 550 ppm $NO + 10\% O_2$ and balance N_2 at a total flow rate of 200 ml/min through the sample bed at 25 °C (or 250 °C) for 2 h. The reactor was purged by N_2 until no NH_3 or NO_x was detected in the effluent. TPD measurements were carried out up to 600 °C with a heating rate of 10 °C/min in N_2 with a flow rate of 200 ml/min.

In situ DRIFTS experiments were conducted with a Nicolet Nexus spectrometer equipped with a liquid nitrogen-cooled MCT detector. A Praying Mantis™ High-Temperature Reaction Chamber from Harrick Scientific Products Inc. was used as the environmental chamber. The fine catalyst powder was placed in a sample cell within an atmospherically controlled chamber. Prior to the test, the catalysts were purged by 20% O_2/N_2 at 450 °C for 30 min, and then cooled to desired temperatures. At each temperature, the background spectrum was collected under nitrogen and was subtracted from the sample spectrum collected at the same temperature.

3. Results and discussion

3.1. Catalytic performance

The catalytic performance of NH_3 -SCR on different catalysts is shown in Fig. 1. Negligible NO_x conversion was observed on CeO_2 -C catalysts at low temperature, and negative NO_x conversion was generated above 300 °C. Meanwhile, slightly higher NO_x conversion was observed on CeO_2 -NS catalysts below 300 °C, and the maximum NO_x conversion reached about 55% around 250 °C. When the reaction temperature was increased above 350 °C, significantly negative NO_x conversions were observed, indicating substantial NO_x formation by catalytic oxidation of NH_3 at high temperatures. Post sulfation of CeO_2 supports, the NH_3 -SCR catalytic performance was significantly improved on both S/CeO_2 -C and S/CeO_2 -NS catalysts. The catalytic results indicated that S/CeO_2 -C catalysts outperformed S/CeO_2 -NS catalysts in a wide range of temperature, exhibiting more than 85% NO_x conversions between 250 and 450 °C. The NO_x conversions of S/CeO_2 -NS catalysts gradually decreased when the temperature went above 350 °C, suggesting that the strong NH_3 oxidation process was still occurring even after sulfation treatment. The reaction rate normalized by BET surface area was calculated when the reaction took place at 200 °C, but not reported when the catalytic conversions were too high (above 250 °C) to avoid operating in a mass transfer limitation regime. The results showed that the specific reaction rate on S/CeO_2 -C catalysts was $0.0101 \mu\text{mol m}^{-2} \text{s}^{-1}$ at 200 °C, which was higher than the corresponding value of $0.0053 \mu\text{mol m}^{-2} \text{s}^{-1}$ on S/CeO_2 -NS catalysts. In addition, the N_2 selectivity of different catalysts was calculated and shown in Fig. 1(b). Only N_2 products were detected on both CeO_2 -C and CeO_2 -NS catalysts below 250 °C. Yet, significant N_2 selectivity loss was observed above 300 °C due to the formation of NO_x and N_2O by-products. For S/CeO_2 -C and S/CeO_2 -NS catalysts, N_2 was the major reaction product in the low-temperature range, and N_2 selectively would slightly decrease above 400 °C due to side reactions of ammonia oxidation. The above results clearly suggest that the intrinsic morphology and sulfation of CeO_2 catalysts significantly influenced the activity and selectivity of NH_3 -SCR performance.

Since NH_3 oxidation might be the main reason that caused performance loss at high temperature, catalytic oxidation of NH_3 was

conducted to gain a better insight of the catalytic performance of different catalysts. As shown in Fig. 2(a), the catalytic performance of NH_3 oxidation ranked in the sequence of CeO_2 -NS > CeO_2 -C > S/CeO_2 -NS > S/CeO_2 -C. CeO_2 -NS catalysts could easily oxidize NH_3 in comparison to the other three catalysts. The NH_3 conversion of CeO_2 -NS gradually increased with increasing temperature and reached total oxidation of NH_3 above 400 °C. The light-off temperature of CeO_2 -C catalysts was around 355 °C, and the catalysts reached total oxidation of NH_3 at 500 °C. In addition, the ability of sulfated CeO_2 catalysts to oxidize NH_3 was significantly inhibited in comparison to non-sulfated CeO_2 catalysts. The light-off temperatures of both S/CeO_2 -NS and S/CeO_2 -C shifted to higher temperatures of approximately 367 °C and 400 °C, respectively. As shown in Fig. 2(b and c), N_2 was the main reaction product for NH_3 oxidation at low temperature, and the selectivity of N_2 at 250 °C would account for 93% and 95% on CeO_2 -NS and CeO_2 -C catalysts, respectively. As the temperature increased to 500 °C, the selectivity of N_2 greatly decreased, and the selectivity of NO_x gradually increased to approximately 83% and 80% for CeO_2 -NS and CeO_2 -C catalysts, respectively. The results indicate that NO_x is the major reaction product of NH_3 oxidation on both CeO_2 -NS and CeO_2 -C catalysts at high temperatures. As shown in Fig. 2(d and e), only N_2 was observed below 350 °C on both sulfated CeO_2 catalysts. Similar to non-sulfated CeO_2 catalysts, the selectivity of N_2 gradually decreased as the temperature increased. The N_2 selectivity of sulfated CeO_2 catalysts was much higher than that of the corresponding non-sulfated CeO_2 catalysts. It implied that NH_3 -SCR reactions would take place on both S/CeO_2 -NS and S/CeO_2 -C catalysts, on which the NO_x products could be further reduced by unoxidized NH_3 to form N_2 . At 500 °C, the N_2 selectivity of S/CeO_2 -C catalysts changed to 77%, which was much higher than 39% on S/CeO_2 -NS catalysts. It can be speculated that S/CeO_2 -C catalysts were much more effective than S/CeO_2 -NS for the NH_3 -SCR reaction at high temperatures, and S/CeO_2 -NS could easily generate much more NO_x during NH_3 oxidation. It should be noted that almost no N_2O product was observed for the two sulfated CeO_2 catalysts during the tests. Generally, the significant difference of NH_3 oxidation activity on CeO_2 -NS and CeO_2 -C catalysts should correlate to the differences in BET surface area of CeO_2 supports (Table 1). CeO_2 nanospheres were composed of many small crystallites and exhibited a large surface area, which could provide a high amount of surface active oxygen species. This greatly improved the catalytic performance of ammonia oxidation. For sulfated CeO_2 catalysts, the formation of surface sulfates and the decrease in BET surface area should be two major factors responsible for the loss of performance during NH_3 oxidation.

As shown in Fig. 3, NO oxidation conversions of different catalysts

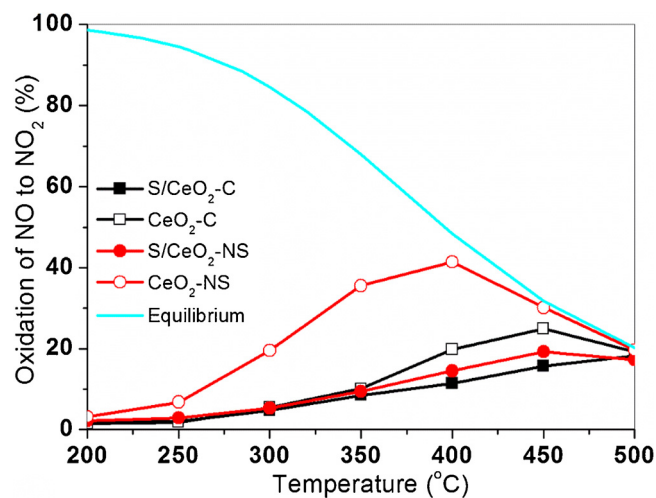


Fig. 3. Catalytic performance of NO oxidation to NO_2 over different catalysts. Reaction conditions: 550 ppm NO , 10% O_2 , balance N_2 , and $WHSV = 90,000 \text{ mL g}^{-1} \text{ h}^{-1}$.

ranked in the sequence of $\text{CeO}_2\text{-NS} > \text{CeO}_2\text{-C} > \text{S/CeO}_2\text{-NS} > \text{S/CeO}_2\text{-C}$, which followed the same trend as the catalytic oxidation of NH_3 . For the most active $\text{CeO}_2\text{-NS}$ catalysts, the NO oxidation conversions gradually increased with increasing reaction temperature and reached a maximum value of 41% at 400 °C, and then decreased when the temperature further increased. The volcano shape of NO oxidation curves is due to the kinetic limitations in the low-temperature range and thermodynamic limitations in the high-temperature range. In comparison to non-sulfated CeO_2 catalysts, $\text{S/CeO}_2\text{-C}$ and $\text{S/CeO}_2\text{-NS}$

catalysts showed much lower NO oxidation ability during the tests, suggesting the NO oxidation performance was greatly inhibited after the formation of surface sulfates.

3.2. Characterization of catalysts

3.2.1. Structural features

The morphology and crystallite size of different catalysts are characterized by TEM techniques. It could be observed from Fig. 4(a–d) that

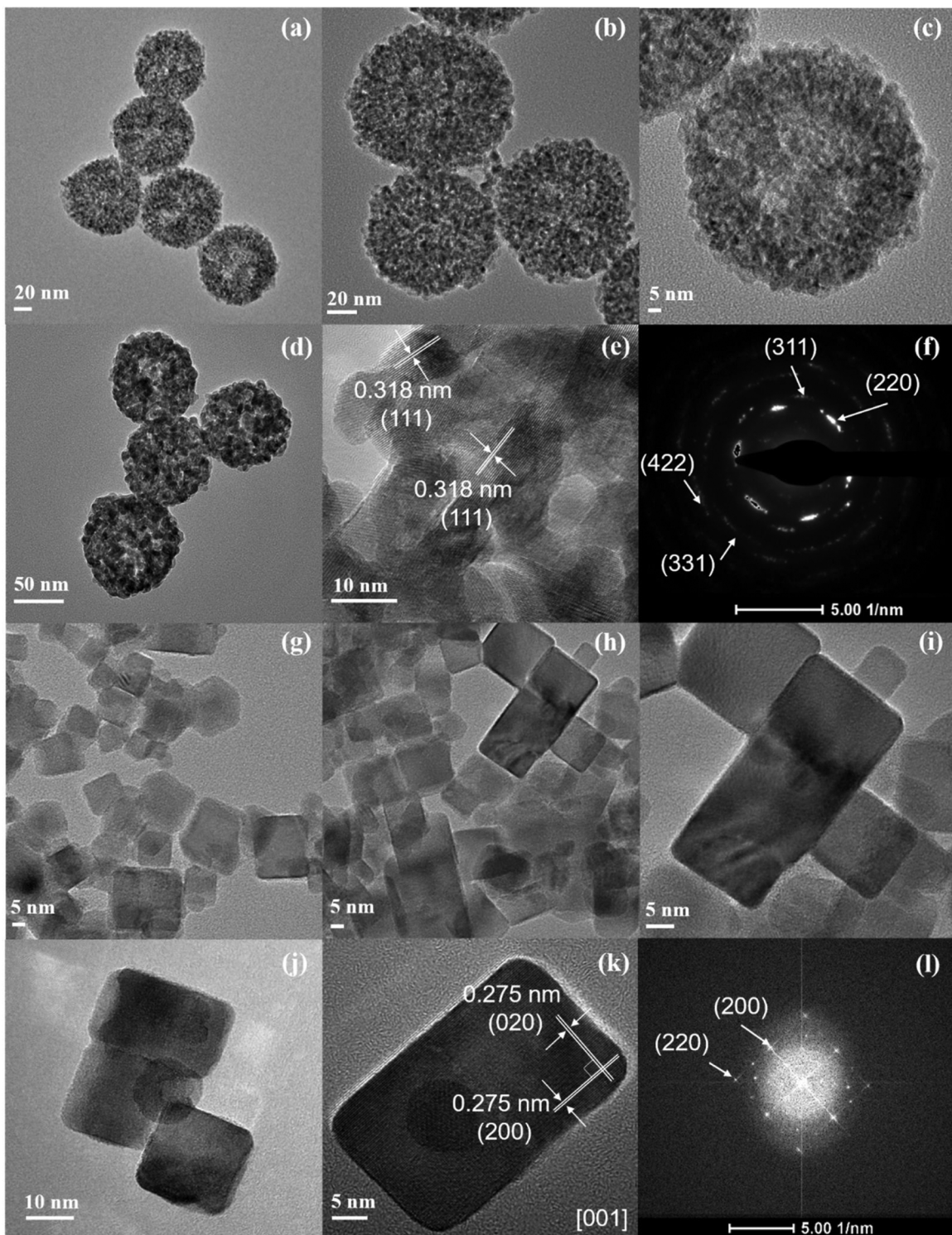


Fig. 4. TEM images at different magnification scales of (a–c) $\text{CeO}_2\text{-NS}$, (d and e) $\text{S/CeO}_2\text{-NS}$, (f) the selected-area electron diffraction (SAED) pattern of $\text{S/CeO}_2\text{-NS}$, (g–i) $\text{CeO}_2\text{-C}$, (j and k) $\text{S/CeO}_2\text{-C}$, and (l) the Fast Fourier Transform (FFT) pattern of $\text{S/CeO}_2\text{-C}$.

both CeO₂-NS and S/CeO₂-NS catalysts exhibited uniform nanosphere structures, which were composed of small crystallites with a particle size of approximately 7–10 nm. It should be noted that, in comparison to fresh CeO₂ nanosphere [22,23], hollow pores and relatively larger crystallites were evident in both CeO₂-NS and S/CeO₂-NS catalysts. This could be caused by the calcination process during catalyst preparation, and the high-temperature treatment could result in the agglomeration of crystallites. As observed in high-resolution TEM images of S/CeO₂-NS (Fig. 4(e)), the d-spacing value was 0.318 nm, close to the (111) lattice spacing of the standard CeO₂ fluorite structure (JCPDS PDF#34-0394). In fact, polycrystalline structures of S/CeO₂-NS catalysts were evinced in the selected-area electron diffraction (SAED) patterns. As shown in Fig. 4(f), multiple bright electron diffraction rings were observed that could be assigned to the diffractions of (220), (311), (331), and (422) crystal planes, respectively. Fig. 4(g–j) shows that both CeO₂-C and S/CeO₂-C catalysts exhibited uniform nanocube structures, implying that sulfation treatment did not significantly change the morphology of CeO₂ cubes. As shown in Fig. 4(k), the HRTEM image shows that the d-spacing was 0.275 nm, which was consistent with the (200) lattice spacing of the standard CeO₂ fluorite structure (JCPDS PDF#34-0394). Both (200) and (220) planes could be identified by corresponding Fast Fourier Transform (FFT) patterns in Fig. 4(l), revealing that the CeO₂ nanocrystal cubes were enclosed by (200) planes.

As shown in Fig. 5, the X-ray diffraction peaks of both CeO₂-C and CeO₂-NS catalysts were consistent with the standard CeO₂ fluorite structure (JCPDS PDF#34-0394) without any impurities. The main diffraction peaks of S/CeO₂-C and S/CeO₂-NS corroborated with the corresponding crystal phases of CeO₂. Three weak diffraction peaks

were also observed at 13.7°, 17.1°, and 20.1°, and could be assigned to the (102), (020), and (022) planes of Ce₂(SO₄)₃ (JCPDS PDF#52-1494), respectively. These results suggested that both S/CeO₂-C and S/CeO₂-NS catalysts were mainly composed of CeO₂ crystallites accompanied by a small amount of Ce₂(SO₄)₃ surface species. Quite evidently, the diffraction peaks of CeO₂-NS catalysts were much broader than those of CeO₂-C catalysts due to the smaller sizes of CeO₂-NS crystallites. According to the calculation by Scherrer equation (Table 1), the average crystallite size of CeO₂-NS catalysts was about 7.7 nm, much smaller than 16.4 nm of CeO₂-C catalysts. The addition of surface sulfates was associated with a slight increase of the crystallite size to 10.4 nm and 17.7 nm for S/CeO₂-NS and S/CeO₂-C, respectively. It can be speculated that the sulfate groups were mainly located on the surface of CeO₂, which would explain the slight increase in the average crystallite sizes.

The porosity and surface area of the as-prepared catalysts were characterized by N₂ adsorption-desorption isotherms. As shown in Fig. 6(a), all the catalysts exhibited type IV isotherms with hysteresis loop of H3 type, indicating the formation of mesoporous structures comprised of non-rigid aggregates of particles [24]. The total adsorbed amount of N₂ of sulfated CeO₂ catalysts was much lower than that of the corresponding non-sulfated CeO₂ catalysts, indicating that sulfation can cause a significant decrease in BET surface area and pore volume. As shown in Table 1, the BET surface area decreased from 40.7 to 15.8 m²/g for CeO₂-C and S/CeO₂-C, respectively. Meanwhile, the values changed from 135.4 to 27.8 m²/g for CeO₂-NS and S/CeO₂-NS, respectively. Fig. 6(b) shows the pore size distributions of different catalysts. Both CeO₂-NS and S/CeO₂-NS exhibited bimodal distribution

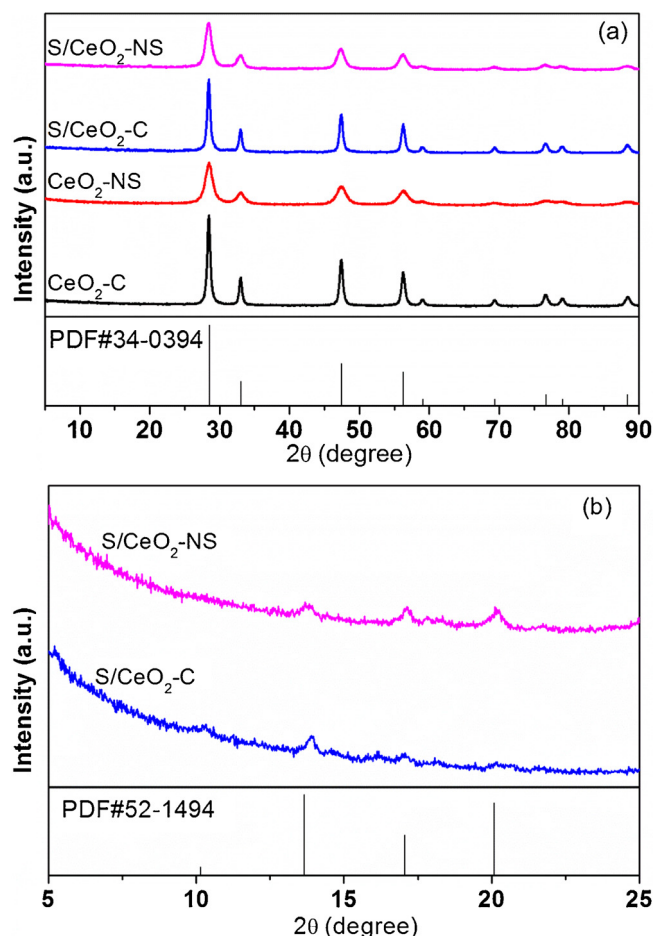


Fig. 5. XRD patterns of different catalysts.

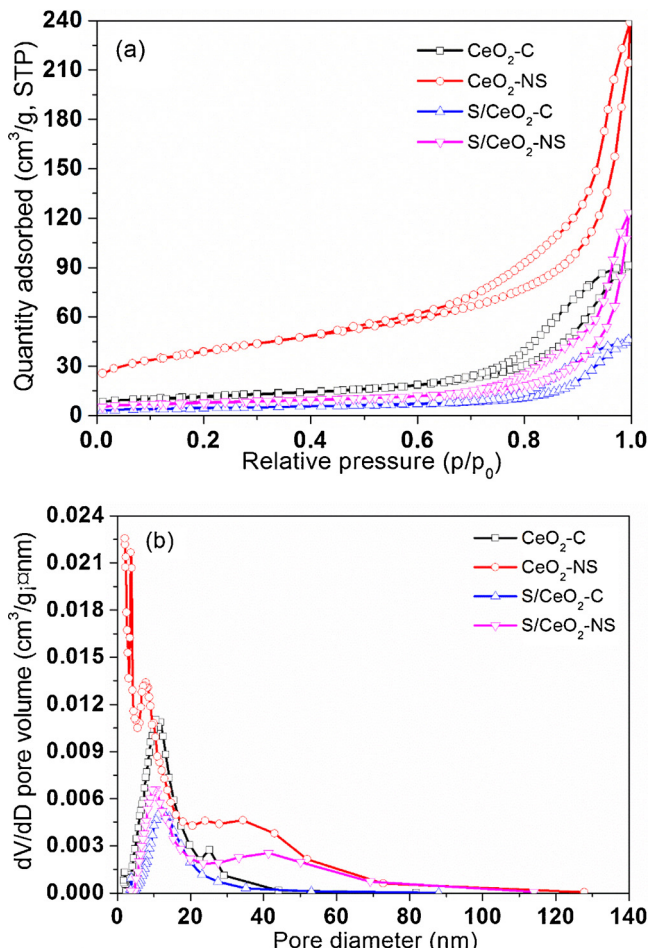


Fig. 6. N₂ adsorption-desorption isotherms (a) and pore size distributions (b) of different catalysts.

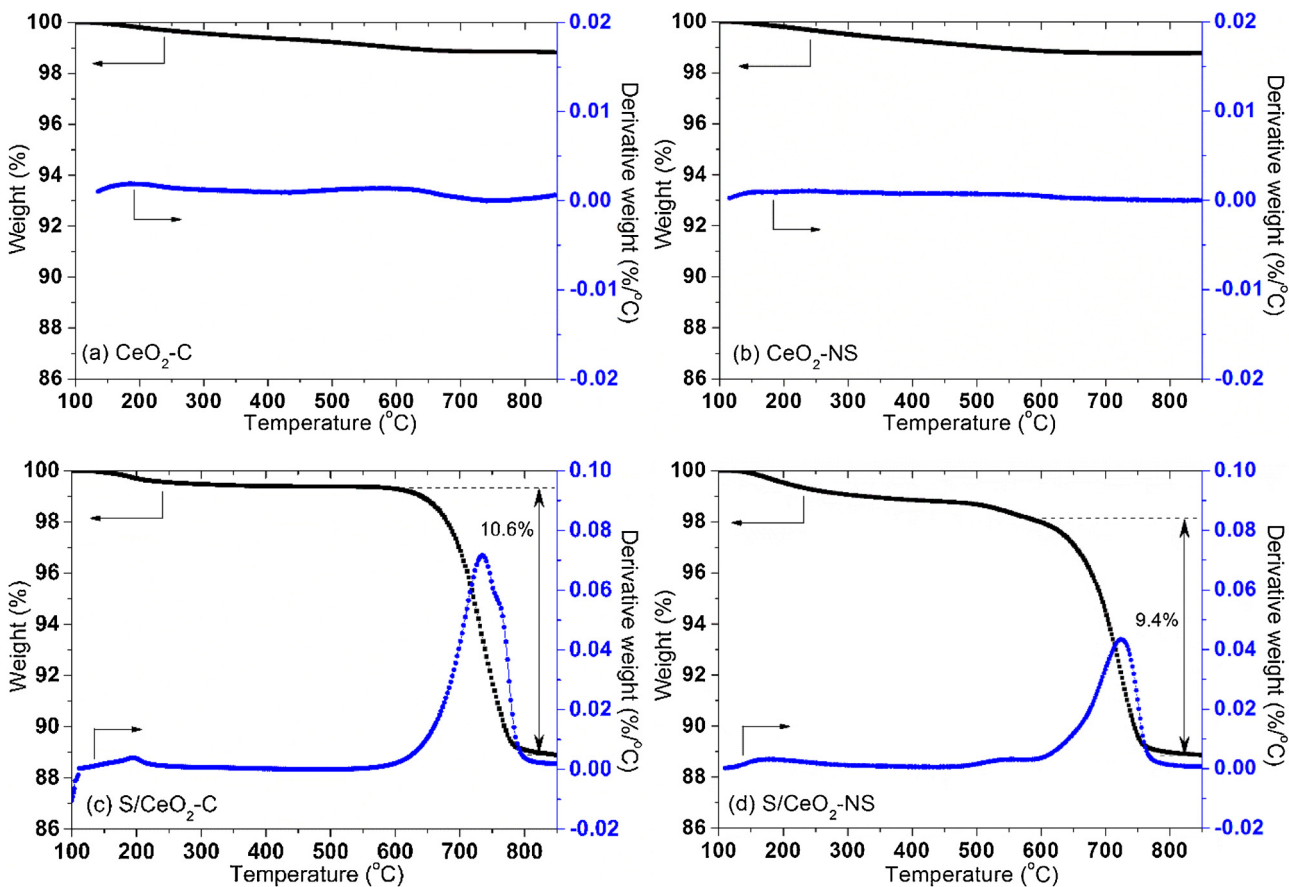


Fig. 7. TGA and DTG curves of different catalysts during thermal treatment in nitrogen (a) $\text{CeO}_2\text{-C}$; (b) $\text{CeO}_2\text{-NS}$; (c) $\text{S/CeO}_2\text{-C}$; (d) $\text{S/CeO}_2\text{-NS}$.

curves, which may be a result of interparticle spacing and hollow pore structures. The pore size of $\text{CeO}_2\text{-NS}$ catalysts was approximately 7.6 nm and 34.4 nm, indicating the formation of mesoporous structures. Post sulfuration treatment, $\text{S/CeO}_2\text{-NS}$ catalysts exhibited slightly larger pores, and the pore sizes increased to 9.8 nm and 41.1 nm. $\text{CeO}_2\text{-C}$ and $\text{S/CeO}_2\text{-C}$ catalysts exhibited similar pore size distributions around 11.1 nm and 12.0 nm, respectively.

TGA technique was further employed for understanding the formation of surface sulfates and the thermal stability of different catalysts. Fig. 7(a and b) shows that the total weight loss for $\text{CeO}_2\text{-C}$ and $\text{CeO}_2\text{-NS}$ catalysts was about 1.6 wt% under N_2 flow. The derivative plots (DTG) transformed from weight loss curves also indicated no significant weight loss in the entire test range. Since the theoretical weight loss should account for approximately 4.6 wt% when CeO_2 decomposed into Ce_2O_3 following Eq. (7), it was speculated that $\text{CeO}_2\text{-C}$ and $\text{CeO}_2\text{-NS}$ were more stable and would not lose the lattice oxygen below 850 °C. The slight weight loss might be ascribed to the desorption of weakly adsorbed surface oxygen. As shown in Fig. 7(c and d), the total weight loss for $\text{S/CeO}_2\text{-C}$ and $\text{S/CeO}_2\text{-NS}$ catalysts was about 11.3% in presence of nitrogen. Meanwhile, a rapid weight loss occurred above 600 °C. The values were 10.6% and 9.4% for $\text{S/CeO}_2\text{-C}$ and $\text{S/CeO}_2\text{-NS}$, respectively. Based on the initial decomposition temperature and weight loss amount, this significant weight loss could correspond to the decomposition of $\text{Ce}_2(\text{SO}_4)_3$ into CeO_2 products according to Eq. (8) [25,26].



3.2.2. Surface properties

The core level photoemission of XPS was used to investigate the surface electronic states of the catalysts. As shown in Fig. 8(a), $\text{Ce}3d$ core level XP spectra were collected, and the deconvolutions of $\text{Ce}3d$ spectra were processed referring to the literature [27,28]. Typically, the $\text{Ce}3d$ spectra are composed of two doublets for Ce^{3+} and three doublets for Ce^{4+} , which are related to the initial states of $3d^{10}4f^1$ and $3d^{10}4f^0$ and various final states caused by the transitions from valence band electrons to $\text{Ce}4f$ states [28]. Therefore, the concentration of Ce^{3+} could be calculated by Eq. (9) [27,28]:

$$c_{\text{Ce}^{3+}} = \frac{v_0 + u_0 + v_1 + u_1}{\sum_i (v_i + u_i)} \quad (9)$$

The quantitative results indicated that the concentrations of Ce^{3+} over $\text{CeO}_2\text{-C}$ and $\text{CeO}_2\text{-NS}$ catalysts were about 17% and 18%, respectively. Meanwhile, much higher concentrations of Ce^{3+} could be detected over $\text{S/CeO}_2\text{-C}$ and $\text{S/CeO}_2\text{-NS}$ catalysts, and the values increased to 27% and 37%, respectively. The improved surface Ce^{3+} concentration should be another sign of the formation of $\text{Ce}_2(\text{SO}_4)_3$ species over sulfated CeO_2 catalysts. The formation of surface $\text{Ce}_2(\text{SO}_4)_3$ species could be further evinced by the high-resolution $\text{S}2p$ spectra in Fig. 8(b). For $\text{S/CeO}_2\text{-C}$ and $\text{S/CeO}_2\text{-NS}$ catalysts, $\text{S}2p$ spectra could be deconvoluted into two components with the binding energy of 169.0 eV ($\text{S}2p_{3/2}$) and 170.1 eV ($\text{S}2p_{1/2}$), corresponding to hexavalent sulfur. The spin-orbit splitting of $\text{S}2p$ was 1.1 eV. The closely spaced spin-orbit components are characteristic of sulfate phases. Thus, it was reasonable to conclude that surface sulfate species were the only forms of sulfur compounds.

01s spectra of $\text{CeO}_2\text{-C}$ and $\text{CeO}_2\text{-NS}$ catalysts exhibited two sub-peaks, which included an intense peak around 529.0 eV, and a faint

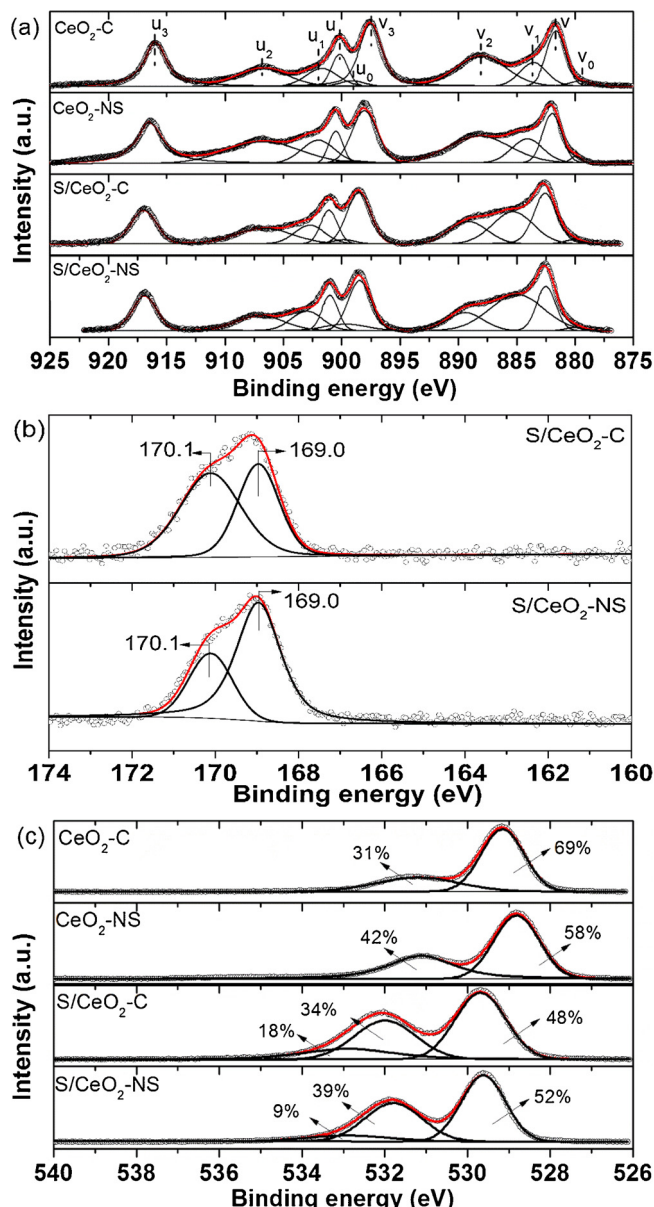


Fig. 8. Peak deconvolutions of (a) Ce 3d, (b) S 2p, and (c) O 1s core lines in X-ray photoelectron spectroscopy for different catalysts.

peak around 531.1 eV. These two peaks could be assigned to lattice oxygen and chemisorbed oxygen on CeO_2 , respectively [29,30]. In addition, three sub-peaks were observed for $\text{S/CeO}_2\text{-C}$ and $\text{S/CeO}_2\text{-NS}$ catalysts. One major sub-peak appeared at approximately 529.7 eV, while two less intense peaks appeared at relatively higher binding energy located around 532.0 eV and 532.9 eV, respectively. These three peaks could be assigned to lattice oxygen, chemisorbed oxygen, and sulfate oxygen ($\text{S}=\text{O}$), respectively [29–31]. Obviously, the third component of sulfate oxygen was only observed on the sulfated CeO_2 catalysts. In comparison to non-sulfated CeO_2 , the appearance of sulfate oxygen species might cause a decrease in the surface concentrations of lattice oxygen on sulfated CeO_2 catalysts.

3.2.3. Reducibility

The catalyst reducibility was evaluated by $\text{H}_2\text{-TPR}$ to elucidate the roles of active oxygen species in the different catalysts. As shown in Fig. 9, $\text{CeO}_2\text{-C}$ catalysts exhibited two reduction peaks. The first peak at 535 °C (starting from 409 °C) could be ascribed to the reduction of

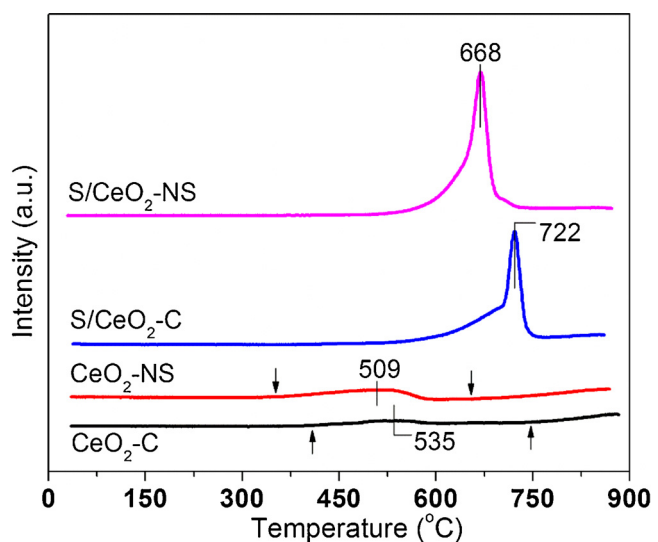
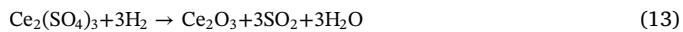
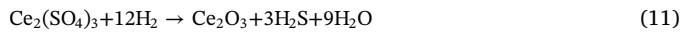


Fig. 9. $\text{H}_2\text{-TPR}$ profiles of different catalysts.

surface oxygen species, and the second peak above 840 °C (starting from 747 °C) was ascribed to the reduction of bulk CeO_2 to Ce_2O_3 by the elimination of oxygen anions from the lattice (Eq. (10)) [32]. For $\text{CeO}_2\text{-NS}$ catalysts, the two reduction peaks significantly shifted towards lower temperatures, and the first peak appeared at 509 °C (starting from 352 °C), indicating an improved reducibility of surface and bulk oxygen coordinated with Ce^{4+} . The improved reducibility of $\text{CeO}_2\text{-NS}$ catalysts might be conflicting with theoretical studies. Based on theoretical work, the formation energy of oxygen vacancies was predicted to follow the sequence of (100) < (111) crystal planes [33]. The reducibility of catalysts is reflected by their ability to release oxygen, therefore the formation energy of oxygen vacancies could be used as a descriptor to indicate the redox ability [34]. Compared to the (111) lattice plane, the (100) lattice plane requires less energy to form an oxygen vacancy, and therefore should be much more reactive towards the redox reaction. However, $\text{CeO}_2\text{-NS}$ catalysts, exposing (111) lattice planes, exhibited improved reducibility in comparison to $\text{CeO}_2\text{-C}$ exposing (100) lattice planes. One could speculate that $\text{CeO}_2\text{-NS}$ catalysts mainly comprised much smaller crystallites, which could facilitate an easier release of the active oxygen species during the reduction process compared to the larger particles in $\text{CeO}_2\text{-C}$ catalysts.

In addition, the reducibility of sulfated CeO_2 catalysts was significantly inhibited in comparison to non-sulfated CeO_2 catalysts, while only one intense reduction peak could be observed that was located at 722 °C and 668 °C for $\text{S/CeO}_2\text{-C}$ and $\text{S/CeO}_2\text{-NS}$ catalysts, respectively. The intense peaks could be assigned to the reduction of surface $\text{Ce}_2(\text{SO}_4)_3$ species. Since no reduction peak of surface oxygen species was observed for sulfated CeO_2 catalysts, it could be speculated that surface oxygen would mainly react with sulfur to form surface sulfates. The hexavalent sulfur in $\text{Ce}_2(\text{SO}_4)_3$ might be reduced into H_2S , S and SO_2 following different pathways as per Eqs. (11)–(13), while the $\text{H}_2/\text{SO}_4^{2-}$ ratio would be 4, 3, and 1, respectively. For this case, the qualitative results indicated that the total amount of H_2 consumption on $\text{S/CeO}_2\text{-C}$ and $\text{S/CeO}_2\text{-NS}$ catalysts was 57 μmol and 68 μmol , respectively. The results were close to the theoretical results of 60 μmol and 83 μmol , respectively, when assuming a $\text{H}_2/\text{SO}_4^{2-}$ ratio of 3 and using the sulfur content determined by ICP-OES techniques. Therefore, elemental S should be the final product after the reduction of $\text{Ce}_2(\text{SO}_4)_3$ in the presence of hydrogen (Eq. (12)). The qualitative results of non-sulfated CeO_2 catalysts are not given here, since the reduction peaks were relatively weak, and could not be accurately calculated.



3.2.4. NH_3 and NO_x adsorption

Fig. 10(a) shows TPD profiles after ammonia adsorption at room temperature on different catalysts. For $\text{CeO}_2\text{-C}$ catalysts, one broad desorption peak was observed at 100°C across the entire desorption temperature range. Meanwhile, one intense peak could be observed around 107°C for $\text{CeO}_2\text{-NS}$ catalysts. This low-temperature desorption peak could be assigned to the physically adsorbed NH_3 and weakly bound NH_3 species adsorbed on Lewis acid sites. Based on the numerical integration of the ammonia desorption peaks, the quantitative results showed total ammonia desorption values of 55 and $160\text{ }\mu\text{mol/g}$ for $\text{CeO}_2\text{-C}$ and $\text{CeO}_2\text{-NS}$ catalysts, respectively. It is believed that the total amount of ammonia desorbed in the low-temperature range was related to the surface area of the catalysts. $\text{CeO}_2\text{-NS}$ catalysts with the larger surface area could easily trap a large amount of ammonia during the adsorption process. For $\text{S/CeO}_2\text{-C}$ and $\text{S/CeO}_2\text{-NS}$ catalysts, there were two ammonia desorption peaks observed around 100°C and 268°C

across the entire temperature range. Similar to ammonia adsorption on non-sulfated CeO_2 catalysts, the low-temperature desorption peaks were ascribed to physically adsorbed NH_3 and weakly bound NH_3 species adsorbed on Lewis acid sites, and the high-temperature peaks could be ascribed to ammonia that desorbed from the Brønsted acid sites. The total amount of ammonia desorption was 138 and $179\text{ }\mu\text{mol/g}$ for $\text{S/CeO}_2\text{-C}$ and $\text{S/CeO}_2\text{-NS}$, respectively. Since the SCR reaction mainly took place above 200°C , the ammonia adsorption processes were also carried out at 250°C . As shown in Fig. S1, a significant amount of ammonia could be observed during the desorption process on the sulfated CeO_2 catalysts, which could be also ascribed to ammonia desorbed from the strong Brønsted acid sites. The desorption peaks of $\text{S/CeO}_2\text{-C}$ and $\text{S/CeO}_2\text{-NS}$ catalysts located at 332°C and 343°C , respectively. Only slight amount of ammonia could be detected on $\text{CeO}_2\text{-NS}$, while no obvious ammonia was detected on $\text{CeO}_2\text{-C}$. The above results implied that sulfation pretreatment greatly affected the surface acidity of the catalysts and changed the surface acidity to Brønsted type. The capacity of ammonia adsorbed over Brønsted acid sites was significantly increased for the sulfated catalysts.

NO_x -TPD test was carried out to acquire information regarding differently adsorbed NO_x species. As shown in **Fig. 10(b)**, two weak NO_x desorption peaks were observed at 313°C and 499°C for $\text{CeO}_2\text{-C}$ catalysts, which might be ascribed to the decompositions of monodentate nitrates and bridging bidentate nitrates, respectively [35,36]. There were three desorption peaks observed on $\text{CeO}_2\text{-NS}$ catalysts. One weak NO_x desorption peak was apparent at 85°C , and two strong NO_x desorption peaks were observed at 376 and 433°C . They could be ascribed to desorption of physically adsorbed NO_x , monodentate nitrates, and bridging bidentate nitrates decompositions, respectively [35,36]. Quantitative results indicated that the total amount of NO_x desorption increased from $40\text{ }\mu\text{mol/g}$ (for $\text{CeO}_2\text{-C}$) to $607\text{ }\mu\text{mol/g}$ (for $\text{CeO}_2\text{-NS}$). Abundant monodentate nitrates and bridging bidentate nitrates appeared over $\text{CeO}_2\text{-NS}$ catalysts due to the strong ability for NO oxidation and the large surface area. In contrast, no obvious decomposition of nitrate species could be observed during the NO_x desorption process for both $\text{S/CeO}_2\text{-C}$ and $\text{S/CeO}_2\text{-NS}$ catalysts. It implied that the NO oxidation process would be greatly inhibited for the sulfated catalysts, which was consistent with the catalytic oxidation of NO results. The total amount of NO_x desorption was $4\text{ }\mu\text{mol/g}$ and $51\text{ }\mu\text{mol/g}$ for $\text{S/CeO}_2\text{-C}$ and $\text{S/CeO}_2\text{-NS}$, respectively.

3.3. Reaction mechanism study by *in situ* DRIFTS

The surface acid sites of different catalysts were first characterized by IR spectra of ammonia adsorption. As shown in **Fig. 11**, two strong bands at 1603 and 1289 cm^{-1} and three weak bands at 1775 , 1468 , 1407 cm^{-1} were observed after ammonia adsorbed on $\text{CeO}_2\text{-C}$ catalysts at room temperature. The two strong bands are due to the bending vibrations of N–H bonds of NH_3 coordinated to Lewis acid sites, while the three weak bands could be due to the bending vibration of NH_4^+ adsorbed on Brønsted acid sites [37–40]. When the temperature gradually increased to 250°C , the intensity of all the bands decreased and even disappeared, implying ammonia desorption from the catalyst surface. Meanwhile, one weak band appeared at 1582 cm^{-1} , which could be ascribed to the formation of surface nitrate species due to ammonia oxidation by lattice oxygen [41,42]. Similarly, $\text{CeO}_2\text{-NS}$ catalysts exhibited two intense bands at 1614 and 1301 cm^{-1} , which was assigned to the bending vibrations of N–H bonds of NH_3 coordinated to Lewis acid sites. Also, most of the bands disappeared when the temperature reached 250°C , and two new bands at 1546 and 1426 cm^{-1} would appear at the same time, indicating the formation of surface nitrate intermediates due to ammonia oxidation [41,42]. It should be noted that amide species in the form of NH_2 (1145 cm^{-1}) produced by NH_3 dehydrogenation were also detected on $\text{CeO}_2\text{-NS}$ catalysts, and these amide species might be considered as reaction intermediates over non-sulfated CeO_2 catalysts [11,38]. In addition, abundant Brønsted

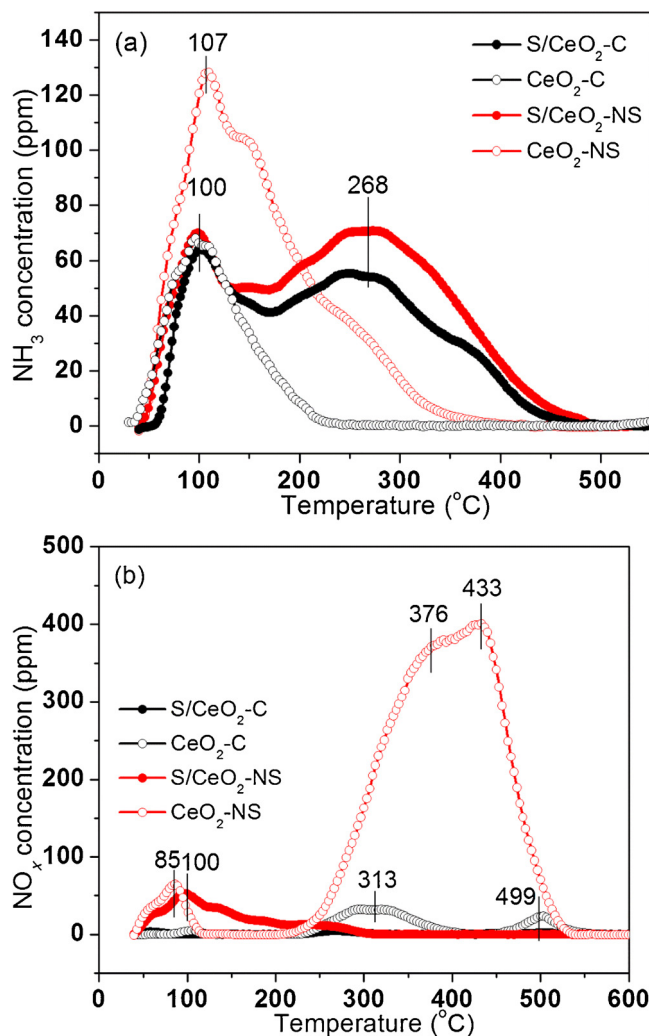


Fig. 10. (a) NH_3 -TPD and (b) NO_x -TPD profiles of different catalysts. Both the adsorption processes were carried out at 25°C .

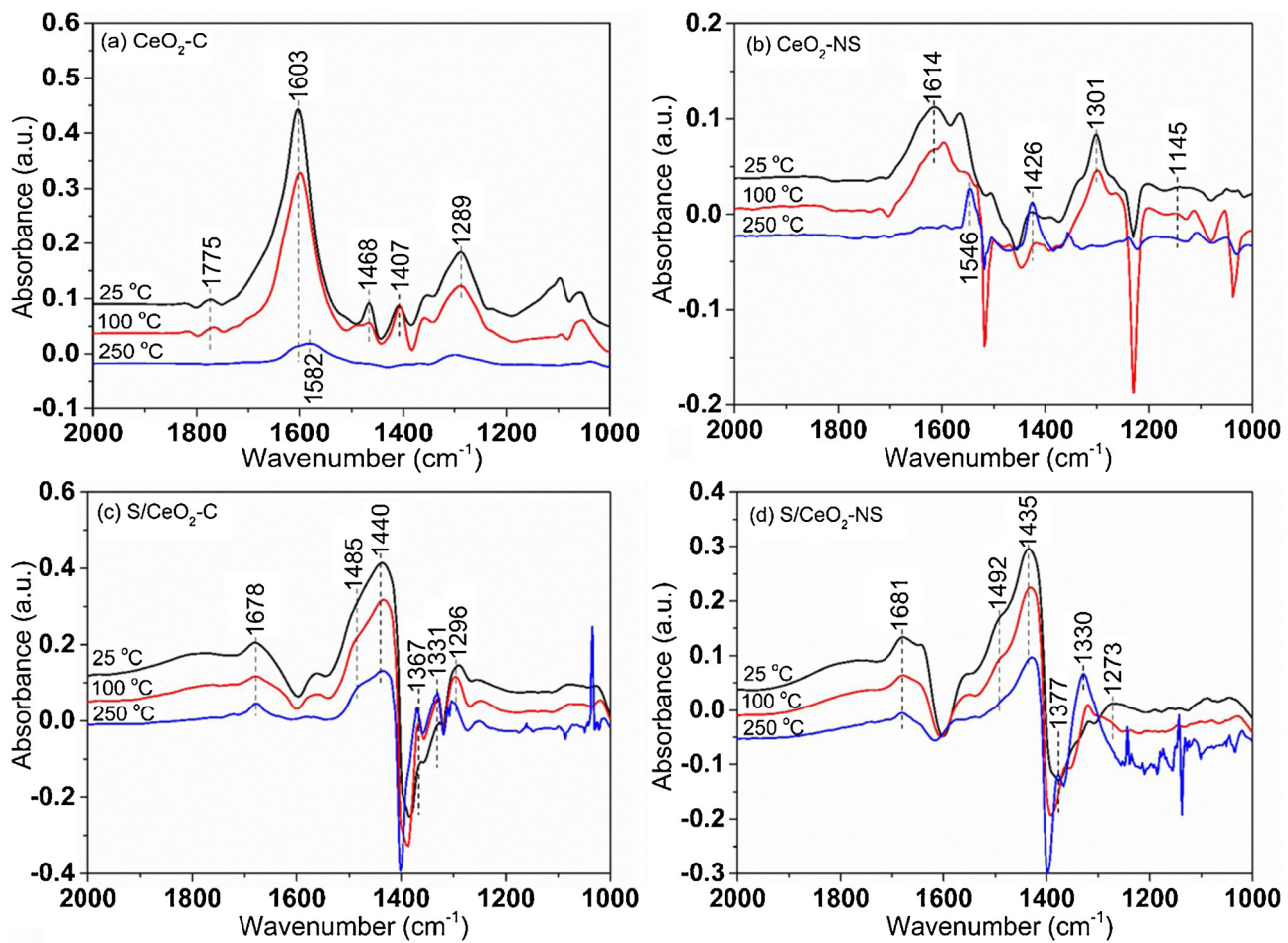


Fig. 11. *In situ* DRIFTS spectra of 550 ppm NH₃ adsorption at 25 °C over different catalysts followed by purging in N₂ at different temperatures.

acid sites were generated after the sulfation treatment of CeO₂ catalysts. Strong bending vibration bands of NH₄⁺ adsorbed on Brønsted acid sites (1440 and 1485 cm⁻¹ for S/CeO₂-C catalysts, and 1435 and 1492 cm⁻¹ for S/CeO₂-NS catalysts) were detected along with weak bending vibration bands of N–H bonds of NH₃ coordinated to Lewis acid sites (1678 and 1296 cm⁻¹ for S/CeO₂-C catalysts, and 1681 and 1273 cm⁻¹ for S/CeO₂-NS catalysts) [11,37–40]. After raising the temperature to 250 °C, a significant amount of NH₄⁺ adsorbed on Brønsted acid sites was still detected on both S/CeO₂-C and S/CeO₂-NS catalysts. Therefore, NH₄⁺ adsorbed on Brønsted acid sites should be much more stable than NH₃ coordinated to Lewis acid sites.

Transient reaction experiment was carried out to further understand the reactivity of the adsorbed ammonia. The catalysts were first saturated with NH₃/N₂ at 250 °C, and then NO + O₂/N₂ was introduced into the sample cell. As shown in Fig. 12, a small amount of adsorbed nitrates (1581 cm⁻¹) were observed after NH₃ adsorption and oxidation on CeO₂-C catalysts [41,42]. After NO + O₂ were fed into the sample cell, different N-containing species quickly formed, which included bridged nitrates (1589 and 1563 cm⁻¹), monodentate nitrates (1460 and 1396 cm⁻¹), and monodentate nitrates (1294, 1240, and 1200 cm⁻¹) [37,43]. Meanwhile, according to the intensity of IR signals, much larger amounts of surface bridged nitrates (1545 cm⁻¹), monodentate nitrates (1373 and 1357 cm⁻¹), and monodentate nitrates (1250 and 1165 cm⁻¹) could be observed on CeO₂-NS catalysts

[37,43]. In contrast, an intense band of NH₄⁺ ions on Brønsted acid sites (1437 cm⁻¹ for S/CeO₂-C and 1429 cm⁻¹ for S/CeO₂-NS) mainly appeared on sulfated CeO₂ catalysts, while several weak bands of NH₃ on Lewis acid sites (1680 cm⁻¹ for S/CeO₂-C and 1681 cm⁻¹ for S/CeO₂-NS) and slight of surface nitrites (1370 cm⁻¹ for S/CeO₂-C and 1376 cm⁻¹ for S/CeO₂-NS) could be observed. After NO + O₂ were introduced into the sample cell, NH₄⁺ ions were significantly consumed, indicating that the reaction took place between adsorbed ammonia species with NO_x in the gas phase. In comparison to non-sulfated CeO₂, almost no surface nitrates and nitrites could be detected on sulfated CeO₂ catalysts. Also, with reaction time passing, a small amount of NO₂ (1620 cm⁻¹ for S/CeO₂-C and 1615 cm⁻¹ for S/CeO₂-NS) was observed on the sulfated CeO₂ catalyst surfaces [39,43]. The above results illustrated that much larger amounts of surface nitrates and nitrites could be detected on the non-sulfated CeO₂ catalysts due to the strong reducibility of Ce⁴⁺. However, ammonia was more readily adsorbed and activated on the sulfated CeO₂ catalysts. Ammonium ions strongly bonded on Brønsted acid sites were detected on the sulfated CeO₂ catalysts and were more reactive with gaseous NO_x in agreement with the Eley-Rideal mechanism.

The reactivity of surface nitrate species was also studied. The catalysts were first treated with NO + O₂ at 250 °C, and then NH₃ was introduced into the sample cell. As shown in Fig. 13, abundant N-containing species were observed on non-sulfated CeO₂ catalysts, and

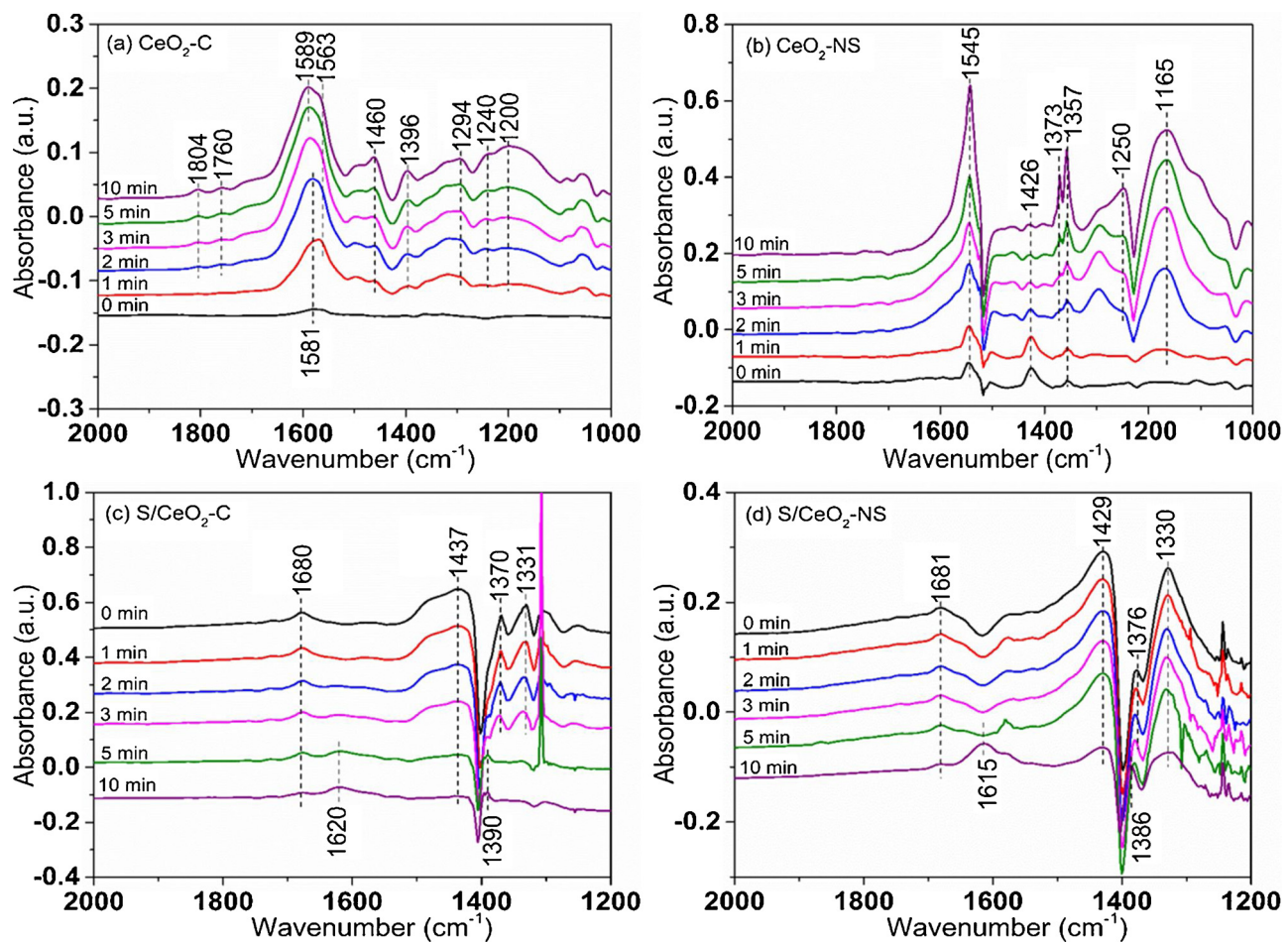


Fig. 12. *In situ* DRIFTS spectra were taken at 250 °C upon passing 550 ppm NO + 10% O₂/N₂ over different catalysts with preadsorbed NH₃.

included bridged nitrates (1597 and 1552 cm⁻¹ for CeO₂-C catalysts, 1568 and 1540 cm⁻¹ for CeO₂-NS catalysts), monodentate nitrites (1461 and 1403 cm⁻¹ for CeO₂-C catalysts, 1498 and 1430 cm⁻¹ for CeO₂-NS catalysts), and monodentate nitrates (1249 and 1200 cm⁻¹ for CeO₂-C catalysts, 1260 and 1198 cm⁻¹ for CeO₂-NS catalysts) [37,39,43]. For both CeO₂-C and CeO₂-NS catalysts, all the bands of surface nitrates did not significantly change when ammonia was fed into the sample cell. The results imply that the surface of non-sulfated CeO₂ catalysts might be fully saturated with nitrates and nitrites, which were very stable and would not react with NH₃ in the gas phase. In contrast, bridged nitrates (1574 and 1533 cm⁻¹ for S/CeO₂-C, 1611 and 1567 cm⁻¹ for S/CeO₂-NS) and monodentate nitrites (1396 cm⁻¹ for S/CeO₂-C, 1394 cm⁻¹ for S/CeO₂-NS) were observed on sulfated CeO₂ catalysts [37,39,43]. For S/CeO₂-C catalysts, NH₄⁺ ions (1480 and 1439 cm⁻¹) on Brønsted acid sites and weak bands of NH₃ (1676 cm⁻¹) on Lewis acid sites gradually formed after NH₃ was introduced [37–40], while the surface nitrates and nitrites were not consumed by gas phase NH₃. The surface of S/CeO₂-NS catalysts might be fully covered by nitrates and nitrites due to the strong redox ability, as no obvious NH₄⁺ ions were observed after feeding ammonia.

As shown in Fig. 14, the steady state reaction of NH₃ + NO + O₂ was conducted on the different catalysts at 250 °C. Evidently, an abundance of bridged nitrates (1595 and 1562 cm⁻¹ for CeO₂-C, 1573 and 1538 cm⁻¹ for CeO₂-NS), monodentate nitrites (1462 and

1399 cm⁻¹ for CeO₂-C, 1491 and 1463 cm⁻¹ for CeO₂-NS), and monodentate nitrates (1245 and 1200 cm⁻¹ for CeO₂-C, 1275 cm⁻¹ for CeO₂-NS) could be detected on non-sulfated CeO₂ catalyst surface. In contrast, after NH₃ + NO + O₂ was fed into the reactor chamber containing the sulfated CeO₂ catalysts, no intense nitrate species were detected, but a small amount of NO₂ (1612 cm⁻¹ for S/CeO₂-C, 1613 cm⁻¹ for S/CeO₂-NS) and monodentate nitrites (1394 cm⁻¹ for S/CeO₂-C, 1403 cm⁻¹ for S/CeO₂-NS) gradually formed.

Based on *in situ* DRIFT spectra, it was hypothesized that NH₃-SCR reaction over CeO₂ and sulfated CeO₂ catalysts should follow the Eley-Rideal mechanism, involving adsorbed ammonia and gaseous NO_x. The NO_x reduction and side reactions in NH₃-SCR reaction could be approximately described as Scheme 1 [38,39,44–46]. Step 1 is the adsorption and dissociation of O₂ on the catalyst surface. Step 2a is the adsorption of gaseous NH₃ on non-sulfated CeO₂ catalyst surface, and Step 2b is the adsorption and activation of gaseous NH₃ on Brønsted acid sites of sulfated CeO₂. The adsorbed NH₃ would be then oxidized to adsorbed NH₂ and NH species by the activated oxygen on surface Ce⁴⁺ sites (Step 3 and 4). At the same time, NO could be also oxidized on surface Ce⁴⁺ sites to gaseous NO₂, surface nitrites, and surface nitrates (Step 5–7). Regarding the NO_x reduction process, adsorbed NH₂ would react with gaseous NO on non-sulfated CeO₂ (Step 8a), while adsorbed NH₄ would react with NO₂ to form the final product of N₂ and H₂O on sulfated CeO₂ (Step 8b). The reaction by-products like NO could be

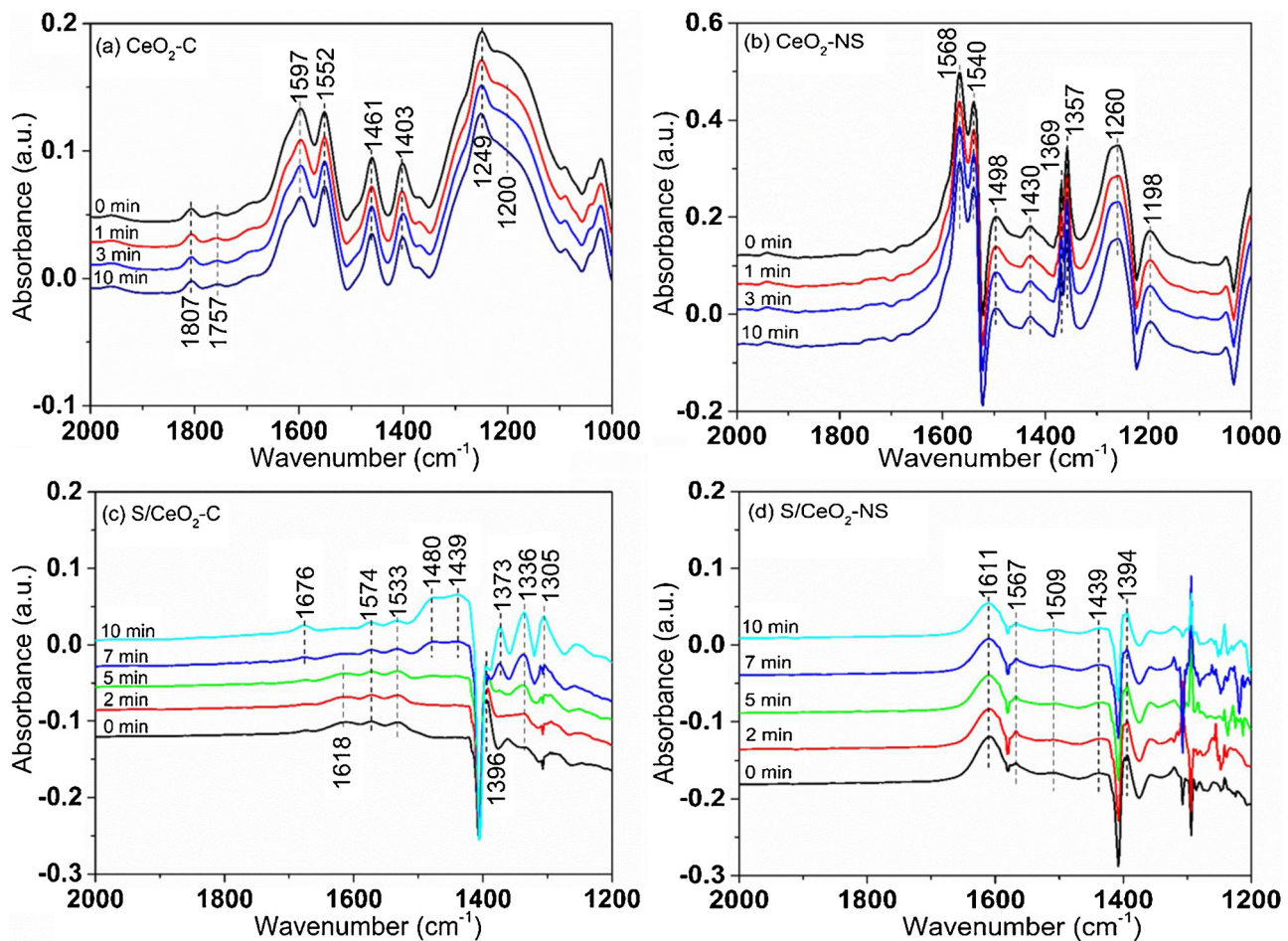


Fig. 13. *In situ* DRIFTS spectra were taken at 250 °C upon passing 550 ppm NH₃/N₂ over different catalysts with preadsorbed NO + O₂.

observed by direct oxidation of adsorbed NH following Step 9, respectively. Surface OH could react with each other to release H₂O and adsorbed surface O (Step 10).

Generally, the activation of ammonia over ceria-based catalysts is a critical step in NH₃-SCR reaction. Adsorbed surface nitrites and nitrates might not be involved in NO_x reduction on either non-sulfated CeO₂ or sulfated CeO₂ catalysts, since all the intensities of the corresponding bands did not diminish after gaseous ammonia was introduced (Fig. 13). For non-sulfated CeO₂ catalysts, it is hypothesized that competitive adsorption and activation of both NO and NH₃ would take place on the same Ce⁴⁺ sites. In comparison to NH₃, gaseous NO_x exhibited a much stronger affinity to Ce⁴⁺, and could be easily activated and transformed to surface nitrites and nitrates (Fig. 14). Compared to CeO₂-C catalysts, CeO₂-NS had smaller crystallite size and larger surface area, which would be beneficial for the collision possibility of NH₃ and NO reactants, and would further improve catalytic performance of NH₃-SCR reaction in the low-temperature range. However, CeO₂-NS with stronger reducibility of Ce⁴⁺ could also facilitate side reactions of NH₃ oxidation, and could generate a large amount of NO_x causing a N₂ selectivity loss in the high-temperature range. As illustrated in Scheme 2, non-sulfated CeO₂ catalysts are Lewis acid solids. The partial positive charge created over cerium due to the electron-withdrawing oxygen groups attracts electron rich species such as ammonia. By sulfation, the acidity of CeO₂ catalyst surface primarily changes to Brønsted type. The

proposed structure of the sulfated CeO₂ is described in Scheme 2, which shows that the surface Ce₂(SO₄)₃ species were mainly comprised of bidentate sulfates. The interaction of water with surface bidentate sulfates can generate Brønsted acid sites. For sulfated CeO₂ catalysts, ammonia is likely to adsorb primarily on Brønsted acid sites, accepting protons from surface Ce₂(SO₄)₃. Meanwhile, NO would still attack Ce⁴⁺ sites and be activated in a similar way as CeO₂ catalysts. The formed NH₄⁺ species would then directly react with NO₂ from the gas phase to form the final products. The proposed reaction Scheme 1 illustrates the activation of NH₃ and NO reactants on separate surface sites, which might be an important cause for the improved NH₃-SCR performance. Also, sulfated CeO₂ would not significantly catalyze NH₃ oxidation due to the inhibited oxidation ability by surface sulfates coordinate with Ce⁴⁺. The limited ammonia oxidation greatly improved the catalytic performance of NH₃-SCR in the high-temperature range.

4. Conclusions

It was demonstrated by employing CeO₂ cubes and nanospheres as NH₃-SCR catalysts that there is a shape-dependence between oxygen vacancies and ammonia oxidation ability. In comparison to CeO₂ cubes, CeO₂ nanospheres with many small crystallites and abundant oxygen vacancies, would facilitate the side reaction of NH₃ oxidation in the NH₃-SCR reaction. After the sulfation treatment, surface Ce₂(SO₄)₃

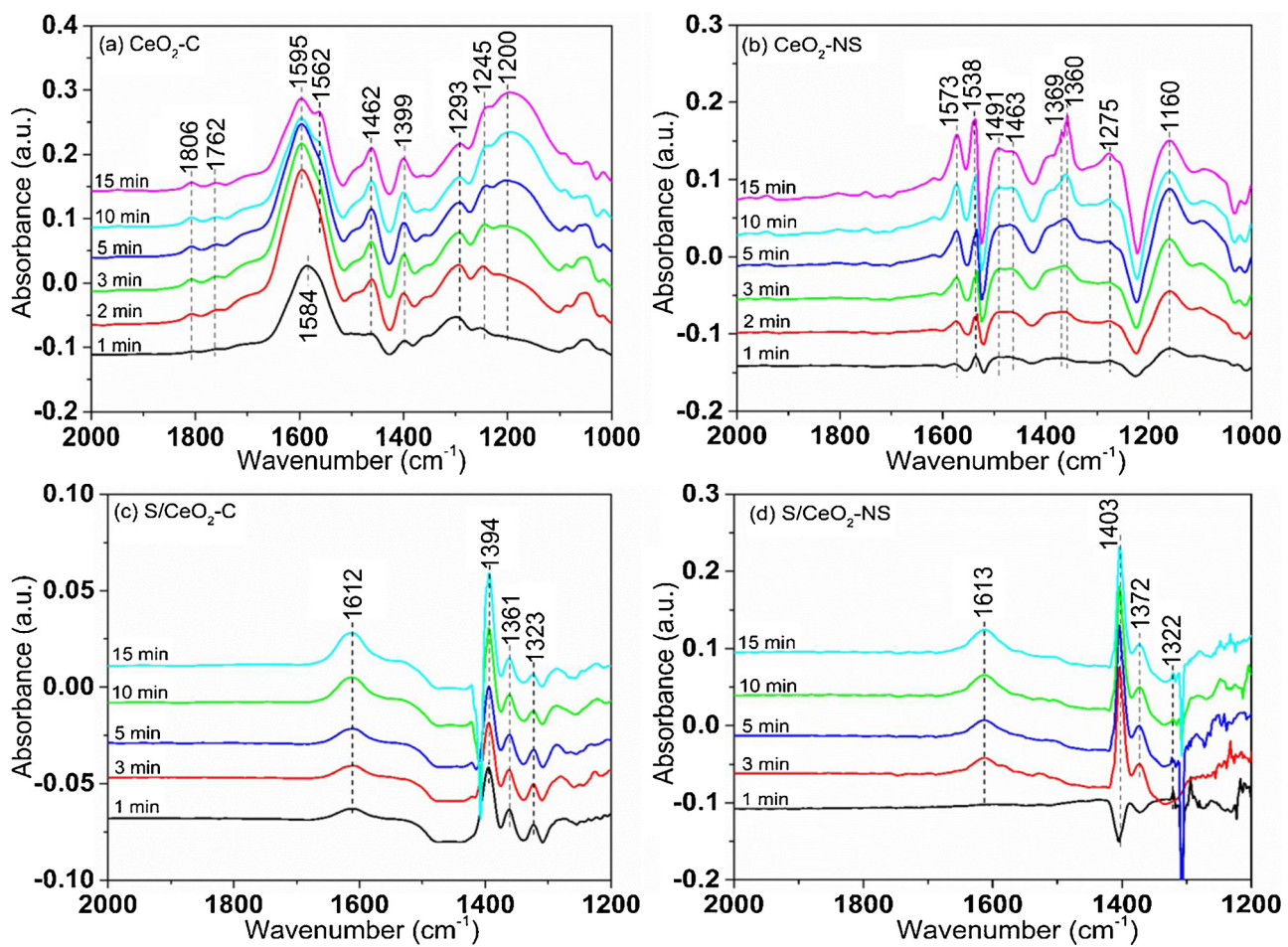
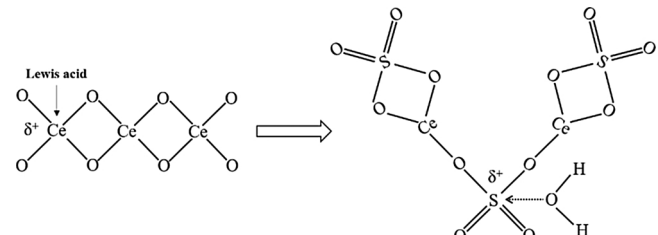


Fig. 14. *In situ* DRIFTS spectra were taken at 250 °C upon passing 550 ppm NH₃ + 550 ppm NO + 10% O₂/N₂ over different catalysts.

species could tune the surface acidity and further facilitate ammonia activation and adsorption in the NH₃-SCR reaction. *In situ* DRIFT spectra suggested that adsorbed NH₂ species should be the key intermediates for CeO₂ catalysts, which react with gaseous NO to form the

1. $O_2 + 2^* \rightarrow 2O^*$
- 2a. $NH_3 + * \rightarrow NH_3^*$
- 2b. $NH_3 + H^* \rightarrow NH_4^*$
3. $NH_3^* + O^* \rightarrow NH_2^* + OH^*$
4. $NH_2^* + O^* \rightarrow NH^* + OH^*$
5. $NO + O^* \rightarrow NO_2 + *$
6. $NO + O^* \rightarrow NO_2^*$
7. $NO_2^* + O^* \rightarrow NO_3^* + *$
- 8a. $NH_2^* + NO \rightarrow N_2 + H_2O + *$
- 8b. $NH_4^* + NO_2 \rightarrow N_2 + 2H_2O + *$
9. $NH^* + 2O^* \rightarrow NO + OH^* + 2*$
10. $2OH^* \rightarrow H_2O + O^* + *$

Scheme 1. Proposed reaction pathways for NH₃-SCR reaction on CeO₂ and sulfated CeO₂.



Scheme 2. The proposed structure of CeO₂ and Ce₂(SO₄)₃ revealing potential acid sites.

final product of N₂ and H₂O. Regarding the NH₃-SCR process over the sulfated CeO₂, NH₄⁺ adsorption on the surface sulfates became more important, and directly reacted with NO₂ that was activated over separate Ce⁴⁺ sites. The high NH₃-SCR performance on sulfated CeO₂ cubes should be related to abundant surface Brønsted acidity and low reducibility of Ce⁴⁺.

Acknowledgments

This work was financially supported by National Key Research and Development Program of China (2017YFC0210701 & 2017YFC0211102) and National Natural Science Foundation of China (51478241). L.M. acknowledges the financial support from international postdoctoral exchange fellowship program (20140054).

Appendix A. Supplementary data

Supplementary material related to this article can be found, in the online version, at doi:<https://doi.org/10.1016/j.apcatb.2018.03.065>.

References

- [1] J. Li, H. Chang, L. Ma, J. Hao, R.T. Yang, Low-temperature selective catalytic reduction of NO_x with NH_3 over metal oxide and zeolite catalysts—a review, *Catal. Today* 175 (2011) 147–156.
- [2] F. Liu, Y. Yu, H. He, Environmentally-benign catalysts for the selective catalytic reduction of NO_x from diesel engines: structure-activity relationship and reaction mechanism aspects, *Chem. Commun.* 50 (2014) 8445–8463.
- [3] H.S. Gandhi, G.W. Graham, R.W. McCabe, Automotive exhaust catalysis, *J. Catal.* 216 (2003) 433–442.
- [4] R.W. McCabe, A. Trovarelli, Forty years of catalysis by ceria: a success story, *Appl. Catal. B: Environ.* 197 (2016) 1.
- [5] W. Shan, F. Liu, H. He, X. Shi, C. Zhang, Novel cerium-tungsten mixed oxide catalyst for the selective catalytic reduction of NO_x with NH_3 , *Chem. Commun.* 47 (2011) 8046–8048.
- [6] L. Chen, J.H. Li, W. Ablikim, J. Wang, H.Z. Chang, L. Ma, J.Y. Xu, M.F. Ge, H. Arandiyani, $\text{CeO}_2\text{-WO}_3$ mixed oxides for the selective catalytic reduction of NO_x by NH_3 over a wide temperature range, *Catal. Lett.* 141 (2011) 1859–1864.
- [7] C. Liu, L. Chen, J. Li, L. Ma, H. Arandiyani, Y. Du, J. Xu, J. Hao, Enhancement of activity and sulfur resistance of CeO_2 supported on $\text{TiO}_2\text{-SiO}_2$ for the selective catalytic reduction of NO by NH_3 , *Environ. Sci. Technol.* 46 (2012) 6182–6189.
- [8] X. Xiao, S. Xiong, Y. Shi, W. Shan, S. Yang, Effect of H_2O and SO_2 on the selective catalytic reduction of NO with NH_3 over Ce/TiO_2 catalyst: mechanism and kinetic study, *J. Phys. Chem. C* 120 (2016) 1066–1076.
- [9] L.J. France, Q. Yang, W. Li, Z. Chen, J. Guang, D. Guo, L. Wang, X. Li, Ceria modified FeMnO_x —enhanced performance and sulphur resistance for low-temperature SCR of NO_x , *Appl. Catal. B: Environ.* 206 (2017) 203–215.
- [10] L. Li, L. Zhang, K. Ma, W. Zou, Y. Cao, Y. Xiong, C. Tang, L. Dong, Ultra-low loading of copper modified $\text{TiO}_2/\text{CeO}_2$ catalysts for low-temperature selective catalytic reduction of NO by NH_3 , *Appl. Catal. B: Environ.* 207 (2017) 366–375.
- [11] S. Yang, Y. Guo, H. Chang, L. Ma, Y. Peng, Z. Qu, N. Yan, C. Wang, J. Li, Novel effect of SO_2 on the SCR reaction over CeO_2 : mechanism and significance, *Appl. Catal. B: Environ.* 136–137 (2013) 19–28.
- [12] H. Chang, L. Ma, S. Yang, J. Li, L. Chen, W. Wang, J. Hao, Comparison of preparation methods for ceria catalyst and the effect of surface and bulk sulfates on its activity toward $\text{NH}_3\text{-SCR}$, *J. Hazard. Mater.* 262 (2013) 782–788.
- [13] Y. Peng, K. Li, J. Li, Identification of the active sites on $\text{CeO}_2\text{-WO}_3$ catalysts for SCR of NO_x with NH_3 : an in situ IR and Raman spectroscopy study, *Appl. Catal. B: Environ.* 140 (2013) 483–492.
- [14] L. Ma, J. Li, R. Ke, L. Fu, Catalytic performance, characterization, and mechanism study of $\text{Fe}_2(\text{SO}_4)_3/\text{TiO}_2$ catalyst for selective catalytic reduction of NO_x by ammonia, *J. Phys. Chem. C* 115 (2011) 7603–7612.
- [15] J.R. Sohn, H.W. Kim, Catalytic and surface properties of ZrO_2 modified with sulfur compounds, *J. Mol. Catal.* 52 (1989) 361–374.
- [16] G.D. Yadav, J.J. Nair, Sulfated zirconia and its modified versions as promising catalysts for industrial processes, *Microporous Mesoporous Mater.* 33 (1999) 1–48.
- [17] K. Wu, L.-D. Sun, C.-H. Yan, Recent progress in well-controlled synthesis of ceria-based nanocatalysts towards enhanced catalytic performance, *Adv. Energy Mater.* 6 (2016) 1600501–1600546.
- [18] K. Zhou, X. Wang, X. Sun, Q. Peng, Y. Li, Enhanced catalytic activity of ceria nanorods from well-defined reactive crystal planes, *J. Catal.* 229 (2005) 206–212.
- [19] K. Zhou, Y. Li, Catalysis based on nanocrystals with well-defined facets, *Angew. Chem. Int. Ed.* 51 (2012) 602–613.
- [20] H.-X. Mai, L.-D. Sun, Y.-W. Zhang, R. Si, W. Feng, H.-P. Zhang, H.-C. Liu, C.-H. Yan, Shape-selective synthesis and oxygen storage behavior of ceria nanopolyhedra, nanorods, and nanocubes, *J. Phys. Chem. B* 109 (2005) 24380–24385.
- [21] Z. Wu, M. Li, S.H. Overbury, On the structure dependence of CO oxidation over CeO_2 nanocrystals with well-defined surface planes, *J. Catal.* 285 (2012) 61–73.
- [22] X. Liang, J.J. Xiao, B.H. Chen, Y.D. Li, Catalytically stable and active CeO_2 mesoporous spheres, *Inorg. Chem.* 49 (2010) 8188–8190.
- [23] L. Ma, D. Wang, J. Li, B. Bai, L. Fu, Y. Li, Ag/ CeO_2 nanospheres: efficient catalysts for formaldehyde oxidation, *Appl. Catal. B: Environ.* 148–149 (2014) 36–43.
- [24] M. Thommes, K. Kaneko, A.V. Neimark, J.P. Olivier, F. Rodriguez-Reinoso, J. Rouquerol, K.S.W. Sing, Physisorption of gases, with special reference to the evaluation of surface area and pore size distribution (IUPAC technical report), *Pure Appl. Chem.* 87 (2015) 1051–1069.
- [25] M.W. Nathans, W.W. Wendlandt, The thermal decomposition of the rare-earth sulphates: thermogravimetric and differential thermal analysis studies up to 1400 °C, *J. Inorg. Nucl. Chem.* 24 (1962) 869–879.
- [26] H. Tagawa, Thermal decomposition temperatures of metal sulfates, *Thermochim. Acta* 80 (1984) 23–33.
- [27] M. Romeo, K. Bak, J. El Fallah, F. Le Normand, L. Hilaire, XPS study of the reduction of cerium dioxide, *Surf. Interface Anal.* 20 (1993) 508–512.
- [28] A. Pfau, K.D. Schierbaum, The electronic structure of stoichiometric and reduced CeO_2 surfaces: an XPS, UPS and HREELS study, *Surf. Sci.* 321 (1994) 71–80.
- [29] J.F. Moulder, W.F. Stickle, P.E. Sobol, K.D. Bomben, *Handbook of X-Ray Photoelectron Spectroscopy*, Published by Perkin-Elmer Corporation, Minnesota, United States of America, 1992.
- [30] W. Xu, H. He, Y. Yu, Deactivation of a Ce/TiO_2 catalyst by SO_2 in the selective catalytic reduction of NO by NH_3 , *J. Phys. Chem. C* 113 (2009) 4426–4432.
- [31] C. Petit, M. Seredych, T.J. Bandosz, Revisiting the chemistry of graphite oxides and its effect on ammonia adsorption, *J. Mater. Chem.* 19 (2009) 9176–9185.
- [32] M. Boaro, M. Vicario, C. de Leitenburg, G. Dolcetti, A. Trovarelli, The use of temperature-programmed and dynamic/transient methods in catalysis: characterization of ceria-based, model three-way catalysts, *Catal. Today* 77 (2003) 407–417.
- [33] M. Nolan, J.E. Fearon, G.W. Watson, Oxygen vacancy formation and migration in ceria, *Solid State Ionics* 177 (2006) 3069–3074.
- [34] M. Aryanpour, A. Khetan, H. Pitsch, Activity descriptor for catalytic reactions on doped cerium oxide, *ACS Catal.* (2013) 1253–1262.
- [35] L. Ma, Y. Cheng, G. Cavataio, R.W. McCabe, L. Fu, J. Li, In situ DRIFTS and temperature-programmed technology study on $\text{NH}_3\text{-SCR}$ of NO_x over Cu-SSZ-13 and Cu-SAPO-34 catalysts, *Appl. Catal. B: Environ.* 156–157 (2014) 428–437.
- [36] F. Liu, K. Asakura, H. He, Y. Liu, W. Shan, X. Shi, C. Zhang, Influence of calcination temperature on iron titanate catalyst for the selective catalytic reduction of NO_x with NH_3 , *Catal. Today* 164 (2011) 520–527.
- [37] G. Ramis, G. Busca, V. Lorenzelli, P. Forzatti, Fourier transform infrared study of the adsorption and coadsorption of nitric oxide, nitrogen dioxide and ammonia on TiO_2 anatase, *Appl. Catal.* 64 (1990) 243–257.
- [38] G. Ramis, G. Busca, F. Bregani, P. Forzatti, Fourier transform-infrared study of the adsorption and coadsorption of nitric oxide, nitrogen dioxide and ammonia on vanadia-titania and mechanism of selective catalytic reduction, *Appl. Catal.* 64 (1990) 259–278.
- [39] G.S. Qi, R.T. Yang, Characterization and FTIR studies of $\text{MnO}_x\text{-CeO}_2$ catalyst for low-temperature selective catalytic reduction of NO with NH_3 , *J. Phys. Chem. B* 108 (2004) 15738–15747.
- [40] R. Farra, S. Wrabetz, M.E. Schuster, E. Stotz, N.G. Hamilton, A.P. Amrute, J. Perez-Ramirez, N. Lopez, D. Teschner, Understanding CeO_2 as a deacon catalyst by probe molecule adsorption and in situ infrared characterisations, *Phys. Chem. Chem. Phys.* 15 (2013) 3454–3465.
- [41] M.A. Larrubia, G. Ramis, G. Busca, An FT-IR study of the adsorption of urea and ammonia over $\text{V}_{2}\text{O}_5\text{-MoO}_3\text{-TiO}_2$ SCR catalysts, *Appl. Catal. B: Environ.* 27 (2000) L145–L151.
- [42] M.A. Larrubia, G. Ramis, G. Busca, An FT-IR study of the adsorption and oxidation of N-containing compounds over $\text{Fe}_2\text{O}_3\text{-TiO}_2$ SCR catalysts, *Appl. Catal. B: Environ.* 30 (2001) 101–110.
- [43] K.I. Hadjilivanov, Identification of neutral and charged N_xO_y surface species by IR spectroscopy, *Catal. Rev.-Sci. Eng.* 42 (2000) 71–144.
- [44] W.S. Kijlstra, D.S. Brands, H.I. Smit, E.K. Poels, A. Bliek, Mechanism of the selective catalytic reduction of NO with NH_3 over $\text{MnO}_x/\text{Al}_2\text{O}_3$, *J. Catal.* 171 (1997) 219–230.
- [45] S. Xiong, Y. Liao, H. Dang, F. Qi, S. Yang, Promotion mechanism of CeO_2 addition on the low temperature SCR reaction over $\text{MnO}_x/\text{TiO}_2$: a new insight from the kinetic study, *RSC Adv.* 5 (2015) 27785–27793.
- [46] S. Yang, F. Qi, S. Xiong, H. Dang, Y. Liao, P.K. Wong, J. Li, MnO_x supported on Fe-Ti spinel: a novel Mn based low temperature SCR catalyst with a high N_2 selectivity, *Appl. Catal. B: Environ.* 181 (2016) 570–580.